

# Surface Emission from Neutron Stars and Implications for the Physics of their Interiors

Feryal Özel

Department of Astronomy, University of Arizona, 933 N. Cherry Ave, Tucson, AZ 85721

E-mail: fozel@email.arizona.edu

**Abstract.** Neutron stars are associated with diverse physical phenomena that take place in conditions characterized by ultrahigh densities as well as intense gravitational, magnetic, and radiation fields. Understanding the properties and interactions of matter in these regimes remains one of the challenges in compact object astrophysics. Photons emitted from the surfaces of neutron stars provide direct probes of their structure, composition, and magnetic fields. In this review, I discuss in detail the physics that governs the properties of emission from the surfaces of neutron stars and their various observational manifestations. I present the constraints on neutron star radii, core and crust composition, and magnetic field strength and topology obtained from studies of their broadband spectra, evolution of thermal luminosity, and the profiles of pulsations that originate on their surfaces.

## Contents

<b>1</b>	<b>Introduction</b>	<b>3</b>
<b>2</b>	<b>Physics of the Neutron Star Surface Emission</b>	<b>5</b>
2.1	Energy Sources . . . . .	5
2.2	Factors determining the flux, spectrum, and the anisotropy of surface emission . . . . .	11
2.3	Atmosphere Models . . . . .	17
2.4	Observed Physical Quantities . . . . .	23
<b>3</b>	<b>A Census of Neutron Star Sources with Surface Emission</b>	<b>25</b>
3.1	Accreting Neutron Stars in Quiescence . . . . .	25
3.2	Accreting Bursting Neutron Stars . . . . .	27
3.3	Accreting Millisecond X-ray Pulsars . . . . .	29
3.4	Rotation-Powered Millisecond Pulsars with Thermal Emission . . . . .	31
3.5	Isolated Cooling Neutron Stars . . . . .	32
3.6	Anomalous X-ray Pulsars and Soft Gamma Ray Repeaters . . . . .	35

<i>CONTENTS</i>	2
<b>4 Neutron Star Radii and Compactness</b>	<b>37</b>
4.1 Neutron Star Structure and Equation of State . . . . .	38
4.2 Spectral Measurements . . . . .	40
4.3 Pulse Profile Fitting . . . . .	43
<b>5 The Composition of the Neutron Star Interior and Its Crust</b>	<b>44</b>
5.1 Comparison of Cooling Models to Thermal Evolution of Isolated Neutron Stars . . . . .	46
5.2 Results for Neutron Star Transients in Quiescence . . . . .	48
<b>6 Neutron Star Magnetic Field Geometry and Evolution</b>	<b>49</b>
<b>7 Complementary Approaches to Neutron Star Physics</b>	<b>51</b>
<b>8 Future Outlook</b>	<b>52</b>

## 1. Introduction

Neutron stars are some of the most fascinating astrophysical objects. During their lifetimes, they are connected to a great variety of phenomena, from the supernova explosions that accompany their births to the bursts of gravitational waves and gamma-rays that are emitted during their inspiral into other compact objects. More than 2000 neutron stars have been discovered to date in the Galaxy with a large diversity of observational appearance from pulsating sources in the radio to bright persistent sources in the X-rays.

Despite their ubiquity, a large number of outstanding problems remain in neutron star physics, owing primarily to the extreme physical conditions present in their interiors and surfaces. Indeed, neutron stars are the stellar objects that possess the most extreme densities and the strongest magnetic fields found in the universe. They also harbor the strongest gravitational fields among all astrophysical objects that still have a surface. Modeling their properties and evolution requires detailed knowledge of physics in regimes that are inaccessible to terrestrial experiments. Conversely, observations of neutron stars offer unique probes of the behavior of matter and radiation in these extraordinary conditions.

Neutron star studies make use of different observables related to the dynamics of binary systems, the structure and energetics of radio pulses, and the spectra and variability properties of their high energy radiation. Among these various probes, direct observations of the emission from a neutron star surface provide the most powerful diagnostic not only of the conditions of its surface but also of its interior composition and physics.

Neutron star surfaces, however, are often hidden from view, as they are overpowered by non-thermal magnetospheric emission in isolated sources or by accretion luminosity in contact binaries. Nevertheless, a remarkable and growing number of sources in different classes show unequivocal evidence for surface emission. During the last 15 years, high energy observatories with superb angular, spectral, and timing resolutions have revealed surface emission from isolated cooling neutron stars (see Ögelman 1995; Page et al. 2009), accreting sources during periods of quiescence (e.g., Degenaar et al. 2011b), thermonuclear bursters (Strohmayer & Bildsten 2006), and isolated neutron stars powered by magnetic field decay (Woods & Thompson 2004). The emission in these different sources probes a wide range of conditions such as temperatures and magnetic field strengths, as well as of spin periods, ages, and evolutionary histories.

Studying the observed surface emission and using it as a tool to understand the properties of neutron stars themselves requires detailed models of their atmospheres, which shape the spectrum and pattern of radiation originating in the stellar crust or core. The great progress in the last decade in detecting surface emission from a variety of neutron stars has been accompanied by the development of atmospheric models that span a wide range of magnetic field strengths, compositions, temperatures, and ionization states. Theoretical models are now routinely compared to high quality

observations, with an emphasis in deriving the fundamental properties of neutron stars from their surface emission.

Observations of neutron stars in quiescence and of neutron stars during thermonuclear bursts have led to the first constraining measurements of neutron star radii. These studies indicate most likely values of  $9 \text{ km} < R < 12 \text{ km}$  and have been used to constrain the equation of state of ultradense matter; equations of state that predict radii as large as 15 km are disfavored by observations (Özel, Baym, & Güver 2010; Steiner, Lattimer, & Brown 2010).

Observations of cooling isolated neutron stars with high sensitivity instruments, which have been modeled with magnetic atmosphere models and used to study the evolution of the thermal properties of neutron stars at different ages, led to significant constraints on neutron star crusts as well as on their interior composition. Comparison of these results with theoretical cooling curves revealed that it is highly unlikely for neutron star cores to have the compositions and the high densities necessary for direct Urca processes to play a role in neutron star cooling (Yakovlev & Pethick 2004). Similar observations of the young neutron star in the supernova remnant Cas A provide tantalizing evidence for the transition to superfluidity in its core (Page et al. 2011; Shternin et al. 2011).

Our understanding of how magnetic fields can power and shape the emission from neutron star surfaces has dramatically advanced thanks to the studies of the highly magnetic Anomalous X-ray Pulsars and Soft Gamma-ray Repeaters (Woods & Thompson 2004). Identifiable effects of ultrastrong magnetic fields both on their thermal spectra and in post-burst phenomena have been observed from these sources. The polarization of the vacuum in strong magnetic fields has been incorporated into neutron star atmosphere calculations that are actively being compared to high energy resolution observations of magnetars in order to definitively identify the signatures of this QED phenomenon.

There has also been significant progress in the past decade on the development of other probes of neutron star gravity and spacetimes, such as the comparison of the observed pulse profiles in accretion powered millisecond pulsars to model lightcurves computed for hotspots on rotating neutron stars. Because the amplitudes and shapes of pulsations are sensitive to the surface gravity, these first studies have been able to place promising constraints on the neutron star masses and radii. These constraints will improve in the near future with the availability of higher signal-to-noise data with new X-ray satellites. It is also eagerly anticipated that the existing probes of neutron star spacetimes will be augmented by observations of gravitational waves and neutrinos emitted from neutron stars to reveal the detailed structure of these compact objects.

In this review, I start by discussing the relevant physical processes that power the surface emission observed from isolated and accreting neutron stars. I then present in Section 2.2-2.4 the various factors that enter models of neutron star atmospheres and determine the flux, the spectrum, and the anisotropy of their surface emission. In Section 3, I summarize the observational properties of numerous types of neutron stars

from which surface emission has been detected, as well as the prevailing models that aim to explain their properties. Sections 4-6 are devoted to discussing in detail how the results on neutron star radii, compositions, as well as magnetic field geometry and evolution are obtained from comparisons of the theoretical models to the observations presented in Section 3. In Section 7, I explore a number of approaches to probing neutron star physics that complement the studies of their surface emission. Finally, I conclude in Section 8 with the prospects for furthering our understanding of neutron star physics through progress in theoretical models as well as with future observations.

## 2. Physics of the Neutron Star Surface Emission

### 2.1. Energy Sources

The surface emission observed from neutron stars can be powered by a variety of physical mechanisms, including the release of the internal heat of the star, accretion, nuclear reactions on the neutron star surface, magnetic field decay, and rotational energy.

### Radiation of residual heat in young neutron stars

Following a supernova explosion, a hot proto-neutron star, with a core temperature of  $\sim 10^{11}$  K, cools through the combination of neutrino emission from its interior and photon cooling from its surface.

Calculations of the thermal evolution of a neutron star after the supernova explosion traditionally divide the object into a stellar interior and an outer heat blanketing envelope that are separated at a boundary radius  $R_b$  that corresponds to a density of  $\sim 10^{10}$  g cm $^{-3}$  (see Yakovlev & Pethick 2004 and Page & Reddy 2006 for reviews of neutron star cooling). The interior becomes isothermal within a few years after the birth of the neutron star, whereas the envelope sustains strong temperature gradients.

The envelope is  $\approx 100$  m deep, has a very short thermal relaxation time and negligible neutrino emissivity. For these reasons, it is modeled as a stationary, plane-parallel envelope in hydrostatic equilibrium. Solving the heat transport equation through this boundary leads to a relation between the temperature  $T_b$  at the bottom of the layer and the effective temperature  $T_{\text{eff}}$  that specifies the radiative flux emerging from the neutron star surface (see below).

Gudmundsson et al. (1982, 1983) modeled the  $T_b - T_{\text{eff}}$  relation and found that it most sensitively depends on the properties of a layer within the envelope where the ions are in liquid phase and the conductivity is determined by electron conduction. Most importantly, if this layer contains an appreciable amount of light elements (up to oxygen), which is allowed given the density and the temperature of the layer, the effective temperature is higher for a given base temperature  $T_b$  (Potekhin et al. 1997). As a result, neutron stars with light elements in this layer are both brighter and have shorter cooling timescales than neutron stars that have only heavy elements in this layer (see Figure 1). The magnetic field in the envelope also has a modest effect on the heat

transport, enhancing it along the field lines and suppressing it in the perpendicular direction. This leads to a non-uniform surface temperature distribution (Greenstein & Hartke 1983; Heyl & Hernquist 1998; Geppert, Küker, & Page 2004). Moreover, for  $B > 10^{11-12}$  G, the effective temperature is slightly enhanced for a given boundary temperature (see Yakovlev & Pethick 2004).

The temperature of the boundary layer is determined by the thermal evolution of the core, which is described in general relativity by the following equations for a spherically symmetric star (Thorne 1977)

$$\begin{aligned} \frac{e^{-\lambda-2\Phi}}{4\pi r^2} \frac{\partial}{\partial r}(e^{2\Phi} L_r) &= -Q - \frac{c_T}{e^\Phi} \frac{\partial T}{\partial t} \\ \frac{L_r}{4\pi \kappa r^2} &= e^{-\lambda-\Phi} \frac{\partial(T e^\Phi)}{\partial r}. \end{aligned} \quad (1)$$

Here  $r$  is the Schwarzschild radial coordinate,  $\Phi$  is the gravitational potential such that  $\exp(\Phi/c^2)$  specifies the gravitational redshift,  $\exp(\lambda) = [1 - 2Gm(r)/rc^2]^{-1/2}$  is the volume correction factor,  $m(r)$  is the mass enclosed within a sphere of radius  $r$ , and  $c$  is the speed of light. In the same equation,  $T$  is the local temperature in the stellar interior,  $Q$  is the neutrino emissivity,  $c_T$  is the heat capacity per unit volume,  $\kappa$  is the thermal conductivity, and  $L_r$  is the local luminosity transported through a sphere of radius  $r$  excluding neutrinos. These equations show that the thermal evolution of the core depends mostly on the heat capacity of the core and the neutrino emissivity. The major contribution to the heat capacity comes from the various degenerate constituents of the core, primarily from non-superfluid neutrons. The heat capacity in a superfluid neutron/proton core is significantly reduced.

The neutrino emissivity depends on the composition and the properties of the stellar interior and is characterized as fast or slow depending on the dominant emission channel. The direct Urca process from nucleons, hyperons, meson condensates, and quark matter leads to fast cooling. Because it has a density threshold, direct Urca operates only in the inner core. It also requires an appreciable proton fraction, which introduces a strong dependence on the equation of state (see Shapiro & Teukolsky 1986; Yakovlev & Pethick 2004 and references therein for a more detailed discussion). Slow neutrino emission, on the other hand, takes place throughout the core of the neutron star via modified Urca and nucleon-nucleon bremsstrahlung processes. The significant effect of baryon superfluidity on neutrino emissivity is discussed in Yakovlev et al. (2001; see references therein). While the presence of a gap in the baryon energy spectrum suppresses the rate of neutrino emission, the formation and breaking of Cooper pairs enhances the neutrino cooling rate.

Models of neutron star cooling fall under three broad categories depending on the relative importance of the neutrino emission processes discussed above. Standard cooling models include only the effects of modified Urca and nucleon-nucleon bremsstrahlung processes (see Pethick 1992), while the minimal cooling paradigm extends standard cooling to include the additional neutrino emission from Cooper pairs in a superfluid core (Page et al. 2004, 2009). Fast cooling models incorporate direct Urca processes

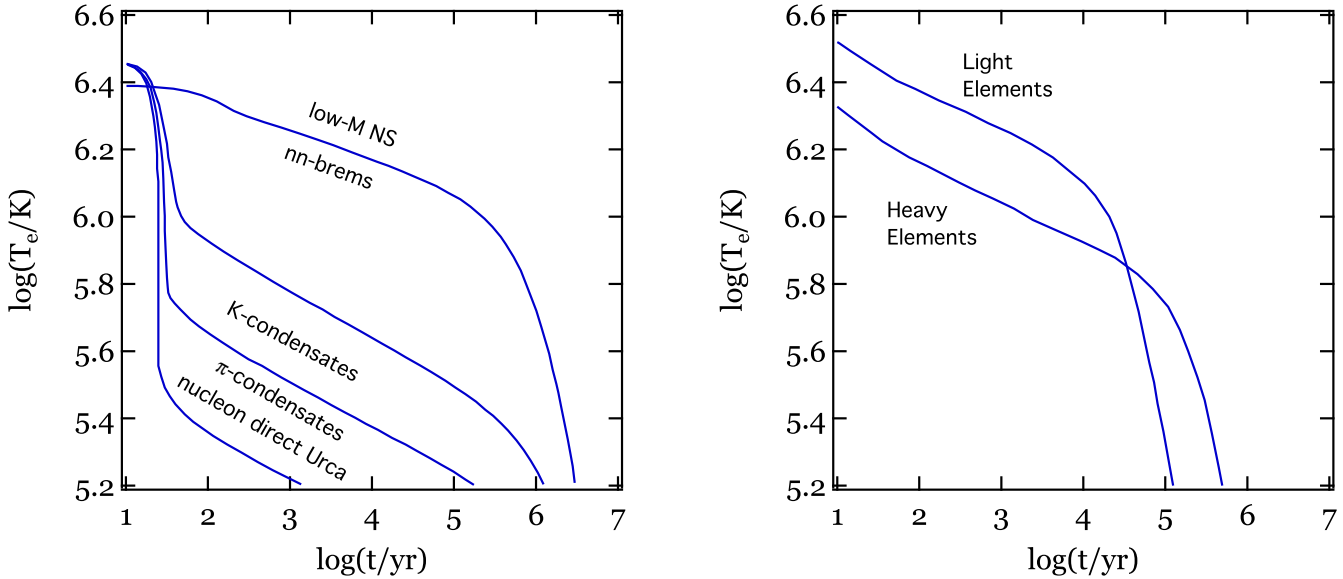


**Figure 1.** (*Left*) Cooling curves showing the fast and slow cooling as a function of neutron star composition and mass, adapted from Yakovlev & Pethick (2004). (*Right*) Cooling curves showing the sensitivity of the cooling rate to the composition of the envelope, adapted from Page et al. (2004). By varying the amount of light elements in the envelope, any trajectory between these two extremes is possible.

and generally result in lower surface temperatures and shorter timescales over which thermal emission from cooling neutron stars is detectable. Examples of cooling curves in Figure 1 show the different cooling rates via these processes for a variety of interior compositions.

The thermal evolution of a neutron star in all models is characterized by three stages. For the first 10–100 years after the birth of the neutron star, the stellar envelope thermally relaxes by radiating its thermal energy and its temperature remains decoupled from that of the core. In the following  $10^5$  years, the temperature of the crust is set by the temperature of the isothermal core, which cools by neutrino emission. During this stage, the neutrino luminosity  $L_\nu$  remains much larger than the photon luminosity  $L_\gamma$  down to a core temperature of  $\text{few} \times 10^8$  K. The heat that diffuses outward from the core to the surface maintains it at a temperature of  $T \sim 10^{5.5-6.5}$  K and gives rise to the thermal emission observed from young neutron stars. Beyond  $10^5$  years, the thermal evolution of the neutron star enters the photon cooling stage during which the neutrino luminosity falls below the photon luminosity and the cooling of the core proceeds via the escape of radiation from the neutron star surface.

The equation of state of the neutron star interior, its superfluidity, and the central density affect the time period over which the thermal emission from the neutron star is observable (see Page et al. 2004). Nevertheless, a large variety of models predict that a young, cooling neutron star is detectable for  $\gtrsim 10^5$  yr in the soft X-rays down to a luminosity of  $\sim 10^{32}$  erg s $^{-1}$ . I will discuss the observations of thermal emission from

young isolated neutron stars in Section 3 and the constraints obtained for the neutron star cooling and interior in Section 5.

### Reradiation of deposited heat between accretion episodes

Electron capture and pycnonuclear reactions occurring primarily at densities  $\sim 10^{12}$  g cm $^{-3}$  in the deep crust of a transiently accreting neutron star release an amount of energy  $Q_{\text{nuc}} \simeq 1.5 - 2$  MeV for each accreted baryon (Haensel & Zdunik 1990, 2008). Brown, Bildsten, & Rutledge (1998) showed that if a fraction  $f$  of this energy is not lost through neutrino emission but is instead deposited as heat in the stellar interior, then these reactions maintain the core at a temperature  $T \sim (5 - 10) \times 10^7$  K. When accretion halts, the envelope relaxes to a thermal equilibrium set by the flux from the hot core and reradiates the deposited energy. Brown et al. (1998) calculated the amount of deposited heat that is thermally reradiated from the core as a function of the time-averaged accretion rate and found

$$L_q \simeq f Q_{\text{nuc}} \frac{\langle \dot{M} \rangle}{m_u} \simeq 9 \times 10^{32} f \frac{Q_{\text{nuc}}}{1.5 \text{ MeV}} \frac{\langle \dot{M} \rangle}{10^{-11} M_{\odot} \text{ yr}^{-1}} \text{ erg s}^{-1} \quad (2)$$

for typical time-averaged accretion rates of  $\sim 10^{-11} M_{\odot} \text{ yr}^{-1}$  inferred for low-mass X-ray transients; here,  $m_u$  is the mass per nucleon. For a storage efficiency  $f = 0.01 - 1$ , this quiescent luminosity is of the same order as the luminosity observed from transient neutron stars during the quiescent phases between high mass accretion episodes, or outbursts, and is, therefore, sufficient to power the quiescent emission (see Section 5.2 and Page & Reddy 2006). (Note that the possible contribution from continued accretion to the luminosity observed during the quiescent phases and the variability in the quiescent luminosity will be discussed in the next section).

### Thermonuclear bursts

In weakly magnetic ( $B < 10^{10}$  G) accreting neutron stars, recurrent X-rays flashes with a rise time of  $\sim 1$  s and a duration of  $\sim 10$  s are frequently observed. During these so-called Type I X-ray bursts, the luminosity emitted from the neutron star surface can dwarf the accretion luminosity by up to two orders of magnitude. This phenomenon has been detected from nearly one hundred neutron stars that accrete hydrogen and helium rich matter from a binary companion (see Galloway et al. 2008 for a recent compilation and Lewin, van Paradijs, & Taam 1993 for an earlier review).

The energy source of these flashes has been identified as the unstable burning of helium via the  $3\alpha$  reaction (sometimes in the presence of hydrogen) in the newly accreted layers on the neutron star surface. Hansen & van Horn (1975) were the first to point out that nuclear burning in shells of fuel on neutron star surfaces are thermally unstable for a wide range of mass accretion rates. The association of Type-I bursts with runaway thermonuclear processes is supported by the agreement between the recurrence time between the flashes ( $\sim$  hours) and the energy generated in each flash (see Joss 1977; Lamb & Lamb 1978).



Thermonuclear flashes are triggered when continued accretion compresses the material accumulating on the neutron star surface, causing a rise in the density and temperature throughout the freshly accreted layer. The recurrence time is set by the ignition conditions at the bottom of this layer, when the rate of energy generation by the  $3\alpha$  reaction,

$$\epsilon_{3\alpha} = 5.3 \times 10^{21} Y^3 \left( \frac{\rho}{10^5 \text{ g cm}^{-3}} \right)^2 \left( \frac{T}{10^8 \text{ K}} \right)^{-3} \exp \left( \frac{-44 \times 10^8 \text{ K}}{T} \right) \text{ erg s}^{-1} \text{ g}^{-1}, \quad (3)$$

which has a very steep dependence on temperature, rapidly exceeds the cooling rate. Here,  $Y$  denotes the helium mass fraction and  $\rho$  and  $T$  denote the density and temperature of the material, respectively.

The consistency between the total energy released per burst and the yield expected from the freshly accreted helium layer is established through an observational comparison between the integrated accretion flux  $F_{\text{accr}}$  and the burst fluence  $\int F_{\text{burst}} dt$  through the parameter  $\alpha$ :

$$\alpha \equiv \frac{\int F_{\text{accr}} dt}{\int F_{\text{burst}} dt}. \quad (4)$$

Theoretically, this is expected to be approximately equal to the ratio of the gravitational potential energy released per nucleon during accretion to the energy released per nucleon,  $E_{\text{nuc}}$ , during thermonuclear burning, i.e.,

$$\alpha \approx \frac{GMm_u}{RE_{\text{nuc}}} = 44 \left( \frac{M}{1.4 M_{\odot}} \right) \left( \frac{R}{10 \text{ km}} \right)^{-1} \left( \frac{E_{\text{nuc}}}{4.4 \text{ MeV nucleon}^{-1}} \right)^{-1}. \quad (5)$$

The distribution of  $\alpha$  values observed from Type I bursts indeed peaks at  $\sim 40$  (see Galloway et al. 2008 for a more detailed discussion).

There are several mass accretion rate regimes that lead to thermonuclear flashes with different characteristics (Fujimoto, Hanawa, & Miyaji 1981; Fushiki & Lamb 1987; Narayan & Heyl 2003). These regimes are typically expressed in units of the Eddington mass accretion rate

$$\dot{M}_{\text{E}} = \frac{8\pi m_p c R}{(1+X)\sigma_{\text{T}}} = 1.8 \times 10^{-8} \left( \frac{R}{10 \text{ km}} \right) \left( \frac{1+X}{1.7} \right)^{-1} M_{\odot} \text{ yr}^{-1}, \quad (6)$$

where  $X$  is the hydrogen mass fraction of the accreted material. Note that the relevant quantity in determining the stability of nuclear burning is the local mass accretion rate per unit area, which has been converted to a total mass accretion rate here by assuming that accretion is uniform over the neutron star surface. At the lowest mass accretion rates,  $\dot{m} = \dot{M}/\dot{M}_{\text{E}} \lesssim 0.01$ , hydrogen burning is unstable and in turn triggers unstable helium burning. At intermediate mass accretion rates,  $0.01 \lesssim \dot{m} \lesssim 0.1$ , hydrogen burns stably into helium between bursts, forming a helium layer at the base of the accreted material. The temperature of the fuel layer rises until the point of helium ignition is reached. At high accretion rates,  $0.1 \lesssim \dot{m} \lesssim 0.9$ , helium ignites unstably in a hydrogen-rich environment because steady burning of hydrogen does not proceed fast enough to convert all of the hydrogen into helium. At even higher mass accretion rates, helium

burning is also stable and thermonuclear flashes are not expected and rarely observed.

### Magnetic field decay

The decay of a very strong magnetic field ( $B > 10^{14}$  G) as well as the release of heat from the stellar crust fracturing under the stress from such a strong field has been suggested as a source of energy for neutron star surface emission (e.g., Arras, Cumming, & Thompson 2004; Aguilera, Pons, & Miralles 2008). This is especially relevant for a group of isolated sources called the Anomalous X-ray Pulsars and the Soft Gamma-ray Repeaters, from which surface emission is observed both as persistent emission in the X-rays and in the aftermath of energetic bursts in the X-ray and  $\gamma$ -ray bands (see Section 3.6).

Several lines of arguments lead to the magnetic fields as the power source. First, if the observed rate of spindown is due to magnetic braking, then the dipolar magnetic field strength at the stellar surface is

$$B = 2 \times 10^{14} \left( \frac{P}{6 \text{ s}} \right)^{1/2} \left( \frac{\dot{P}}{10^{-11} \text{ s s}^{-1}} \right)^{1/2} \text{ G} \quad (7)$$

for these neutron stars, given that their spin periods cluster in the 5 – 12 s range while their period derivatives are measured to be  $\dot{P} \sim 10^{-11} \text{ s s}^{-1}$  (Kouveliotou et al. 1998; see also Section 3, and the review by Woods & Thompson 2004). Note that in individual sources, significant variations in the period derivatives are measured and, therefore, these dipole magnetic field strengths are only approximate (see also the discussion in Section 6 and Figure 13).

Second, the observed persistent luminosity,  $L_X \approx 10^{34-36} \text{ erg s}^{-1}$ , significantly exceeds the spindown power

$$\dot{E}_{\text{rot}} = I\Omega\dot{\Omega} = 1.8 \times 10^{33} \left( \frac{I}{10^{45} \text{ g cm}^2} \right) \left( \frac{\dot{P}}{10^{-11} \text{ s s}^{-1}} \right) \left( \frac{P}{6 \text{ s}} \right)^{-3} \text{ erg s}^{-1}, \quad (8)$$

where  $I$  is the moment of inertia of the neutron star. Deep searches for companions or accretion disks around these neutron stars (e.g., Hulleman et al. 2001; Wang, Kaspi, & Higdon 2007) rule out accretion as the source of energy for the persistent emission or the bursts (but see the arguments for the contribution from accretion in Ertan et al. 2007, 2009).

Finally, the luminosity during bursts is much higher than the persistent luminosity, with  $E \sim 10^{44} \text{ erg}$  released over several hundred seconds, with a pronounced peak within roughly the first second. The radiative fluxes during the bursts are highly super-Eddington and require either that the radiating plasma is confined, most likely magnetically, and/or that the photon-electron scattering cross sections are radically reduced by the presence of a strong magnetic field, up to 4 orders of magnitude below the non-magnetic Thomson cross section (Paczynski 1992; Ulmer 1994; Miller 1995).

The mechanisms for magnetic field decay (e.g., Goldreich & Reisenegger 1992), the resulting heating rate, as well as the properties of neutron star surface emission and thermal evolution have been investigated in a variety of settings (e.g., Arras et al. 2004;

Aguilera et al. 2008). These studies have found that energy injection due to field decay is consistent with the luminosities and the durations of thermal emission observed from these strongly magnetic neutron stars.

### Particle bombardment onto polar caps

Relativistic electron-positron pairs produced in the magnetospheres of pulsars bombard the polar caps on the neutron star surface. The polar caps, heated as a result of the particle bombardment, reradiate this energy as thermal emission peaked in the UV to X-ray wavelengths (Ruderman & Sutherland 1975; Arons 1981; Zhang & Harding 2000; Harding & Muslimov 2001).

An order-of-magnitude estimate for the bombardment rate can be obtained by considering a density of charges in the magnetosphere given by the Goldreich-Julian model (1969), moving at the speed of light, incident on the polar cap that has a radius  $R_p$  (Zhang & Harding 2000),

$$\dot{N} = c N_{\text{GJ}} \pi R_p^2 \approx 10^{30} \left( \frac{R}{10^6 \text{ cm}} \right)^3 \left( \frac{B}{10^{12} \text{ G}} \right) \left( \frac{P}{1 \text{ s}} \right)^{-2} \text{ s}^{-1}. \quad (9)$$

If the positrons have an average Lorentz factor of  $\gamma$ , then the rate of energy deposition in the polar cap is proportional to the bombardment rate and this average Lorentz factor. The detailed calculations of the Lorentz factors as well as of the rate of energy deposition depend on the structure of the pulsar magnetosphere and in the mechanism of particle acceleration, both of which require numerical modeling (see, e.g., Zhang & Harding 2000). Under reasonable assumptions, these models can account for the polar cap emission observed in the X-rays from a small number of rotation-powered pulsars.

### 2.2. Factors determining the flux, spectrum, and the anisotropy of surface emission

In nearly all situations discussed above, energy generation occurs in the neutron star crust or in its core, at depths larger than the scale height of its atmosphere. The only exception is the case of bombardment of the surface by magnetospheric particles, in which energy is deposited throughout the neutron star atmosphere.

The observational appearance of a neutron star is determined, however, by the physical processes that take place in the outermost layer of its surface, which we call the photosphere. The photosphere reprocesses the radiation that originates from the deeper layers and determines the spectrum, anisotropy, and polarization of the radiation that reaches a distant observer.

Modeling this surface emission is usually carried out under the assumption of hydrostatic equilibrium in the atmosphere. This assumption is valid as long as the flux of radiation emitted from the neutron star does not lead to a force that exceeds the gravitational force on the surface. Defining the local Eddington limit as the luminosity at which the radiation and gravitational forces are in balance,

$$L_{\text{Edd}} = \frac{8\pi GMm_p c}{(1 + X)\sigma_T}, \quad (10)$$

provides a useful condition on the validity of the hydrostatic equilibrium assumption: as long as the radiative flux remains below the corresponding Eddington flux, the hydrostatic equilibrium condition is satisfied.

The very large gravitational acceleration on the neutron star surface,

$$g \approx GM/R^2 \approx 1.9 \times 10^{14} \left( \frac{M}{1.4 M_\odot} \right) \left( \frac{R}{10 \text{ km}} \right)^{-2} \text{ cm s}^{-2}, \quad (11)$$

leads to a very small scale height for its atmosphere,

$$h \approx 2 \frac{k_B T}{m_p g} \simeq 8.8 \left( \frac{T}{10^7 \text{ K}} \right) \left( \frac{R}{10 \text{ km}} \right)^2 \left( \frac{M}{1.4 M_\odot} \right)^{-1} \text{ cm}, \quad (12)$$

where  $T$  is the temperature in the atmosphere,  $k_B$  is the Boltzmann constant,  $m_p$  is the mass of the proton, and the material is taken to be fully ionized. This scale height is clearly much smaller than the radius of the neutron star and justifies the approximation of a plane parallel atmosphere that is usually employed in calculations.

The timescale over which photons exchange energy with matter in the photosphere can be estimated as

$$t_e = \frac{\frac{\rho}{m_p} k_B T}{\chi F} \quad (13)$$

where the numerator is the thermal energy per unit volume in the atmosphere,  $\chi$  is the extinction coefficient, and  $F = L/4\pi R^2$  is the flux of radiation through the atmosphere such that the denominator measures the rate of energy exchange. If we take the Thompson cross section to be a characteristic scale for the extinction coefficient, this timescale becomes

$$t_e = 4\pi R^2 \frac{k_B T}{\sigma_T L} \simeq 2.6 \times 10^{-8} \left( \frac{R}{10 \text{ km}} \right)^2 \left( \frac{T}{10^7 \text{ K}} \right) \left( \frac{L}{10^{36} \text{ erg s}^{-1}} \right) \text{ s}. \quad (14)$$

which is much shorter than the characteristic timescale in which the interior cools. This is true even in the case of thermonuclear bursts which occur closest to the surface layers and have cooling times of the order of a few seconds. Because of this, the outermost layers of the star are in radiative equilibrium, characterized by constant flux  $F$ . Frequently, the constant flux is given in terms of an equivalent effective temperature defined as  $\sigma_B T_{\text{eff}}^4 = F$ , where  $\sigma_B$  is the Stefan-Boltzmann constant.

In radiative equilibrium, the constant flux of radiation that diffuses outward from the deep layers determines the temperature gradient in the atmosphere via the relation

$$F_\nu = -\frac{4\pi}{3} \left( \frac{1}{\chi_\nu} \frac{\partial B_\nu}{\partial T} \right) \left( \frac{dT}{dz} \right), \quad (15)$$

which is formally valid in the high optical depth limit. Here,  $\chi_\nu$  is the energy dependent extinction (absorption plus scattering) coefficient,  $B_\nu$  is the blackbody function, and all quantities have been evaluated in the local frame. The extinction coefficient, in turn, depends on the composition of the neutron star surface, its density profile, and its magnetic field strength. As a result, the radiation emerging from the surface in total depends on four parameters: the effective temperature, the gravitational acceleration at

the surface, the composition, and the magnetic field strength. Note that any of these parameters may vary across the neutron star surface, including the gravitational acceleration when the neutron star is oblate due to fast spin.

### Surface Composition

The composition of the neutron star surface is determined by three different processes in the formation and the subsequent life of the star: the abundance and amount of fallback material during the supernova explosion at birth, the abundance and amount of material accreted from a binary companion or from the interstellar medium, and the gravitational settling of the heavy elements.

Assuming that there is no continuing accretion, the time it takes for an element of atomic number  $A = 2Z$  to sediment through an atmosphere of atomic hydrogen on the neutron star surface is (Brown, Bildsten, & Chang 2002 and references therein)

$$t_{\text{sed}} \approx 10^5 \left( \frac{g}{10^{14} \text{ cm s}^{-2}} \right)^{-2} \left( \frac{\rho}{10^5 \text{ g cm}^{-3}} \right)^{1.3} \left( \frac{T}{10^7 \text{ K}} \right)^{0.3} Z^{-0.7} \text{ s}. \quad (16)$$

The density at an electron scattering optical depth of  $\tau_T$  is given by hydrostatic equilibrium and scales as

$$\rho = \frac{gm_p^2\tau_T}{2\sigma_T k_B T} = 1.5 \left( \frac{g}{10^{14} \text{ cm s}^{-2}} \right) \left( \frac{T}{10^7 \text{ K}} \right)^{-1} \left( \frac{\tau_T}{10} \right) \text{ g cm}^{-3}. \quad (17)$$

Inserting this density into the expression for the sedimentation timescale, we find

$$t_{\text{sed}} = 0.013 \left( \frac{g}{10^{14} \text{ cm s}^{-2}} \right)^{-0.7} \left( \frac{T}{10^7 \text{ K}} \right)^{-1.6} \left( \frac{\tau_T}{10} \right)^{1.3} \left( \frac{Z}{8} \right)^{-0.7} \text{ s}. \quad (18)$$

As a result, even an element as light as oxygen can remain in the photosphere and give rise to atomic lines in the neutron star spectrum only if there are either no lighter elements present or if it is being continuously replenished by accretion or by convection, e.g., from the deeper layer where thermonuclear bursts take place.

Light elements are expected to be present on the neutron star surface either by fallback or by accretion from a binary companion or from the interstellar medium. In the case of accretion, light elements can also be produced by spallation even if the accreted material consists entirely of heavy elements (Bildsten et al. 1992). The amount of hydrogen that is necessary to cover the surface of a neutron star down to its photosphere can be estimated, for a non-magnetic neutron star, by

$$m_H = 4\pi R^2 h N_p m_p \quad (19)$$

where  $h$  is the scale height of the hydrogen layer above the photosphere and the gas is assumed to be ionized so that the hydrogen density is equal to the proton density,  $N_H = N_p$ . For simplicity, if we take the electron density  $N_e$  to be constant down to an electron scattering optical depth of unity, i.e.,  $\tau = N_e \sigma_T h$ , then the mass of hydrogen needed becomes

$$m_H = 1.6 \times 10^{-20} \left( \frac{\tau}{1} \right) \left( \frac{R}{10 \text{ km}} \right)^2 M_\odot, \quad (20)$$

which is indeed a very small amount of hydrogen. Even for magnetic neutron stars where the scattering cross section is significantly reduced (see below), so that the depth of the layer down to an optical depth of unity in the X-ray band can be 5-6 orders of magnitude larger, less than  $10^{-10} M_{\odot}$  of hydrogen accreted from the interstellar medium, a companion, or during the supernova explosion is sufficient to provide a light element atmosphere that determines the formation of the surface spectrum.

The typical mass accretion rates for neutron stars in contact binaries ranges from  $10^{-11} M_{\odot} \text{ yr}^{-1}$  to  $10^{-8} M_{\odot} \text{ yr}^{-1}$ . Clearly, it takes a trivial amount of time for the required amount of hydrogen to be accumulated on the neutron star surface in this situation. We can also estimate the amount of time it takes for a neutron star to accrete this amount of hydrogen from the interstellar medium. Using the Bondi-Hoyle formalism, the mass accretion rate is given by

$$\dot{M}_{\text{BH}} = \frac{4\pi(GM)^2 \rho_{\text{ISM}}}{v^3}, \quad (21)$$

where  $\rho_{\text{ISM}}$  is the density of the interstellar medium and  $v$  denotes the spatial velocity of the neutron star. (Note that accretion rates in realistic situations, as predicted by detailed numerical models, often have additional scalings; see Ruffert 1996 and the discussion in Perna et al. 2003). For typical values of the parameters of the interstellar medium and of the neutron star velocities (Arzoumanian et al. 2002), the mass accretion rate becomes

$$\dot{M}_{\text{BH}} = 10^{-17} \left( \frac{M}{1.4 M_{\odot}} \right)^2 \left( \frac{\rho_{\text{ISM}}}{2 \times 10^{-24} \text{ g cm}^{-3}} \right) \left( \frac{v}{100 \text{ km s}^{-1}} \right) M_{\odot} \text{ yr}^{-1}. \quad (22)$$

The timescale for the accretion of sufficient hydrogen to cover the stellar surface, therefore, ranges between  $\ll 1$  yr for a non-magnetic neutron star to  $\sim 10^3$  yr for a highly magnetic one (in which the photosphere occurs at larger column densities, see below), unless there is a physical reason, such as the propeller mechanism (Illarionov & Sunyaev 1975; Romanova et al. 2004), that inhibits accretion onto the neutron star surface. Coupled with the short timescale for the sedimentation of heavy elements, this result justifies the dominant use of hydrogen and helium compositions when modeling the emission from neutron star surfaces.

### Magnetic Field Strength

The magnetic field of a neutron star has profound effects on the properties of its surface and, therefore, on the emission originating from it. Magnetic field strengths can vary between  $< 10^{8-9}$  G in steadily accreting or recycled neutron stars to  $\sim 10^{15}$  G in magnetars (see the census of sources in the next section). The lower end of this range is considered “unmagnetized” due to the negligible effect of the magnetic field on the properties of the plasma, the hydrodynamics, the structure of the atoms, or the photon-electron interaction cross sections. In the upper end of this range, on the other hand, the magnetic force dominates over the other forces at play in the surface layers (with the exception of gravity) and becomes the most important parameter that determines the emission properties.

The electron cyclotron energy

$$E_{cycl,e} = \frac{\hbar e B}{m_e c} = \hbar \omega_{c,e} = 11.6 \left( \frac{B}{10^{12} \text{ G}} \right) \text{ keV} \quad (23)$$

is a natural unit to use when quantifying the strength and the effects of the magnetic field because it can easily be compared to the electron rest energy, the Fermi energy, the Coulomb energy, and the thermal energy of the matter in the surface. For example, even at the fairly modest field strength of  $10^{12}$  G, the cyclotron energy exceeds by an order of magnitude the typical surface thermal energies of  $\lesssim 1$  keV. The field strength at which the cyclotron energy equals the electron rest energy defines the quantum critical field

$$B_Q \equiv \frac{m_e^2 c^3}{e \hbar} = 4.4 \times 10^{13} \text{ G}, \quad (24)$$

beyond which we find a regime in which new physical processes start to take place. Finally, comparison of the electron cyclotron energy to the characteristic energy scale in the atom  $E_{\text{atom}} = 1 \text{ Ryd} = e^2/(2a_0) = 13.6 \text{ eV}$ , where  $a_0$  is the Bohr radius, helps define the regime in which the cyclotron energy significantly exceeds the typical Coulomb energy. This happens at a field strength  $B \simeq 1.2 \times 10^9 \text{ G}$ , above which magnetic field effects considerably alter the properties of atoms and molecules.

At  $E_{\text{cycl}} \leq E_{\text{atom}}$ , a perturbative treatment of the effects of the magnetic field gives rise to the well-known Zeeman splitting of atomic energy levels. In the opposite regime, Coulomb forces act as a perturbation to magnetic forces. The electrons are confined to the ground Landau level and the Coulomb force binds the electrons along the magnetic field direction. This results in two important changes in the atomic structure: the atoms become cylindrical and the spacing between the energy levels becomes larger. A simplified treatment for the hydrogen atom gives 160 eV for the ground state energy at  $10^{12}$  G and 540 eV at  $10^{14}$  G, compared to 13.6 eV for the non-magnetic case (see the review of Harding & Lai 2006 and references therein for the approximations and a detailed discussion).

The cylindrical atoms can form covalent bonds along the magnetic field direction to make up linear molecular chains, which in turn can form three dimensional condensates. The corresponding dissociation energies are smaller than the ionization energies and scale as  $E_{\text{dis}} = [\ln(E_{\text{cycl}}/E_{\text{atom}})]^2$ .

Last but not least, the magnetic field strength drastically affects the propagation of photons through the neutron star atmosphere and hence the photon-electron interaction cross sections. Because the electrons are confined to the ground Landau level in the direction perpendicular to the magnetic field, the interaction cross sections exhibit a very strong dependence on polarization and the direction of propagation. In most circumstances, photon propagation can be described in terms of two orthogonal polarization modes. The cross section for the so-called extraordinary (or perpendicular) mode, which describes the case where the electric field vector of radiation is perpendicular to the magnetic field, is suppressed by a factor  $(E/E_b)^2$  with respect to the non-magnetic case; see Figure 2. The cross section for the ordinary (parallel) mode

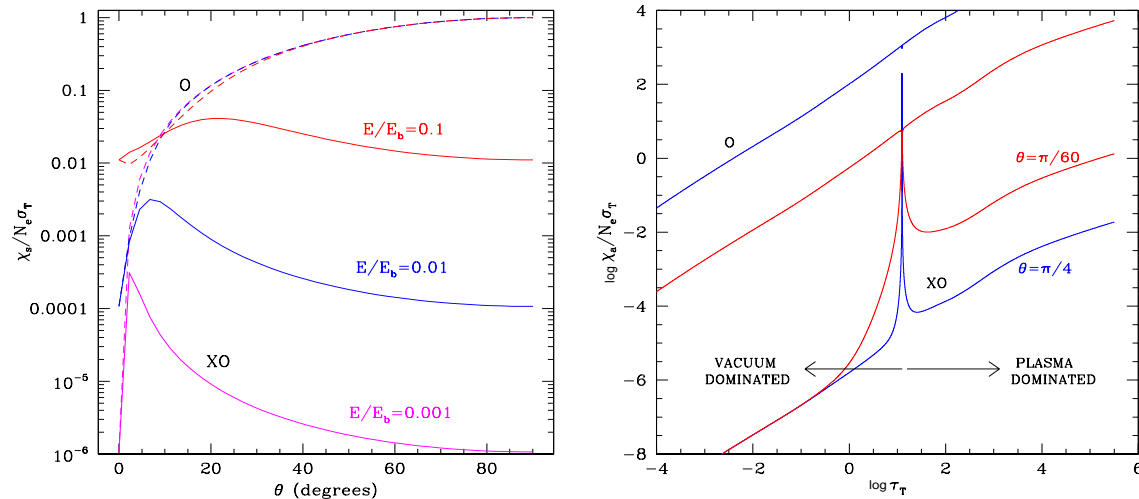


**Figure 2.** (Left) The extinction coefficient for scattering for the extraordinary (solid line) and the ordinary (dashed line) modes as a function of the direction of propagation  $\theta$  with respect to the magnetic field orientation, for different values of the photon energy  $E$  in units of the cyclotron energy, which is denoted here as  $E_b$ . (Right) The absorption coefficients of the extraordinary (XO) and ordinary (O) modes as a function of Thomson optical depth in the atmosphere of a neutron star for two directions of propagation, for a photon energy of 0.5 keV in a  $10^{15}$  G magnetic field (adapted from Özel 2001). For each mode, the two curves show different directions of photon propagation with respect to the magnetic field. The sharp feature at  $\log \tau_T \simeq 1$  occurs at the transition from plasma-dominated to vacuum-dominated interaction cross sections.

remains comparable to the non-magnetic case for direction of propagation perpendicular to the magnetic field orientation but is also suppressed when the photons are propagating along the field (Gnedin & Pavlov 1974; Pavlov & Shibano 1979; Özel 2001; Ho & Lai 2001; van Adelsberg & Lai 2006).

The interaction of the photons with the electrons and protons in the magnetic atmosphere is characterized by strong resonances at the cyclotron energy, which leads to potentially detectable absorption features in the surface spectra. The electron cyclotron energy is given in equation (23) and falls within the 0.5-10 keV X-ray band, where neutron star surface emission is often detected, if the magnetic field strength is between  $5 \times 10^{10}$  G to  $10^{12}$  G (see section 2.4 for a discussion of gravitational redshifts). The cyclotron energy for the protons is a factor  $m_p/m_e$  higher than the electron cyclotron energy. Therefore, for a proton cyclotron feature to fall in the soft X-ray band, the surface magnetic field needs to be between  $10^{14}$  G to  $2 \times 10^{15}$  G.

One other process that influences the propagation of photons in the outermost layers of a neutron star atmosphere in a strong magnetic field is the polarization of the magnetic vacuum itself. When the plasma density is low, the photons interact primarily with virtual electron-positron pairs in the vacuum. The polarization of the



virtual pairs in the presence of the strong magnetic field leads to a significant change in the permeability and dielectric tensor of the vacuum with a magnitude that scales as  $(B/B_Q)^2$  (Adler 1971). Because of this dependence, vacuum polarization effects are significant at field strengths  $B \gtrsim B_Q$ . In the presence of a plasma with a density gradient, which is characteristic of neutron star atmospheres, vacuum polarization gives rise to a resonance when the normal modes of photon propagation change from being mostly circularly polarized at high electron densities (deeper in the atmosphere) to being mostly linearly polarized at low densities. Thus, at a critical density that depends on photon energy, the conversion of photons between the two polarization modes is highly enhanced, accompanied by a change in the opacities of the normal modes (Adler 1971; Tsai & Erber 1975; Mezaros & Ventura 1979; Kaminker et al. 1982; see Mezaros 1992 for a review). These resonances modify the emerging spectrum and give rise to broad absorption-like features (Bulik & Miller 1997; Özel 2001, 2003; Lai & Ho 2002).

### 2.3. Atmosphere Models

The properties of the radiation emerging from a neutron star surface have been investigated in different settings, taking into account the various considerations of flux, composition, and magnetic field strength discussed above. Emission models, such as those discussed below, typically employ as parameters the effective temperature  $T_{\text{eff}}$ , magnetic field strength  $B$ , and surface gravity  $g$ , in addition to specifying the composition of the material making up the atmosphere.

The justification of the frequently employed assumptions of plane-parallel geometry, radiative equilibrium, and hydrostatic equilibrium conditions were discussed in the previous section. The ionization state of the atmosphere is determined by solving the (magnetic) Saha equation. We can broadly classify the results depending on the effective temperature of the atmosphere and the magnetic field of the neutron star.

In weakly magnetic neutron stars and at high effective temperatures, e.g., in the atmospheres of bursting neutron stars, the thermal energy  $E_{\text{th}}$  is much larger than the ionization energy  $E_{\text{ion}}$  for the lighter elements as well as the majority of the (possibly present) heavier elements, causing them to be ionized. Only a few ionization states of heavy elements may survive. In non-magnetic neutron stars with lower surface temperatures, on the other hand, most heavy elements remain neutral or at low ionization states, leading to numerous features in the spectra from atomic transitions (see Figure 3). In isolated sources with high magnetic field strengths, such as magnetars, a competition between the high ionization energies and the high temperatures/densities at the photosphere determine the ionization equilibrium. Due to suppressed cross sections, the photosphere reaches deeper in the atmosphere where temperatures can reach  $\sim 1$  keV and particle densities  $N \sim 10^{29} \text{ cm}^{-3}$ . Thus, despite the larger energies required for ionization in strong magnetic fields, the ionized fractions usually remain high for light elements.

The ionization state of the atmosphere and the magnetic field strength determine

the relevant processes that need to be taken into account in the solution of the radiative transfer equation. These include electron scattering, free-free emission and absorption (Bremsstrahlung), as well as bound-bound and bound-free atomic transitions where applicable. The cross sections of interactions depend on the temperature profile of the atmosphere, which, in turn, needs to be determined self consistently with the radiation field for the radiative equilibrium condition to be satisfied. Iterative techniques such as lambda iteration, complete linearization, or Lucy-Unsöld scheme are utilized to achieve consistency between the temperature profile and the radiation field (see, e.g., Mihalas 1978 for a description of these interactions and numerical techniques).

### Spectrum of the Surface Emission

Figure 3 shows representative spectra of radiation emerging from neutron star atmospheres under different physical conditions. Four cases are shown: non-magnetic, cool neutron stars ( $T_{\text{eff}} = 10^{4.7-6.5}$  K; Zavlin et al. 1996); cool neutron stars with moderate magnetic field strengths ( $B = 2 \times 10^{11} - 10^{13}$  G; Shibano et al. 1992), hot bursting neutron stars with different metallicities (Suleimanov et al. 2011), and strongly magnetic neutron stars (Özel 2003).

The characteristic feature of all model neutron star spectra is a deviation from the blackbody function of the same effective temperature. Because of the strong energy dependence of the free-free and bound-free absorption coefficients, the depth of the photosphere increases with increasing photon energy. As a result, radiation that emerges at higher photon energies originates deeper in the atmosphere where the temperature is also higher. This causes a hardening and broadening of the spectrum compared to a black body at the effective temperature. Such distortions are often characterized by a parameter called the color correction factor defined as

$$f_c = \frac{T_{\text{BB}}}{T_{\text{eff}}}, \quad (25)$$

where  $T_{\text{BB}}$  is the temperature obtained from fitting the spectrum with a blackbody. The hardening and broadening in the spectra give rise to color correction factors that are in the range  $1 \lesssim f_c \lesssim 1.8$ . Color correction factors near the low end of this range are rare in model spectra and are almost always caused by the presence of broad and/or numerous absorption lines (see, e.g., the upper left panel of Figure 3).

All atmosphere models satisfy the radiative equilibrium condition by employing iterative schemes between the radiation field and the temperature and density in the atmosphere. Different numerical models rely on a variety of numerical techniques to achieve this and often implement convergence criteria with different levels of precision. In addition, there are variations between how the effects of neutron star surface gravity are taken into account, i.e., whether the macroscopic properties of the neutron star and the surface gravity are allowed to vary consistently. Finally, there exist some differences in the physical processes taken into account in separate calculations, which may involve making simplifying assumptions, e.g., in the treatment of angular redistribution in scattering, or accounting for additional physics such as electron conduction. Because of

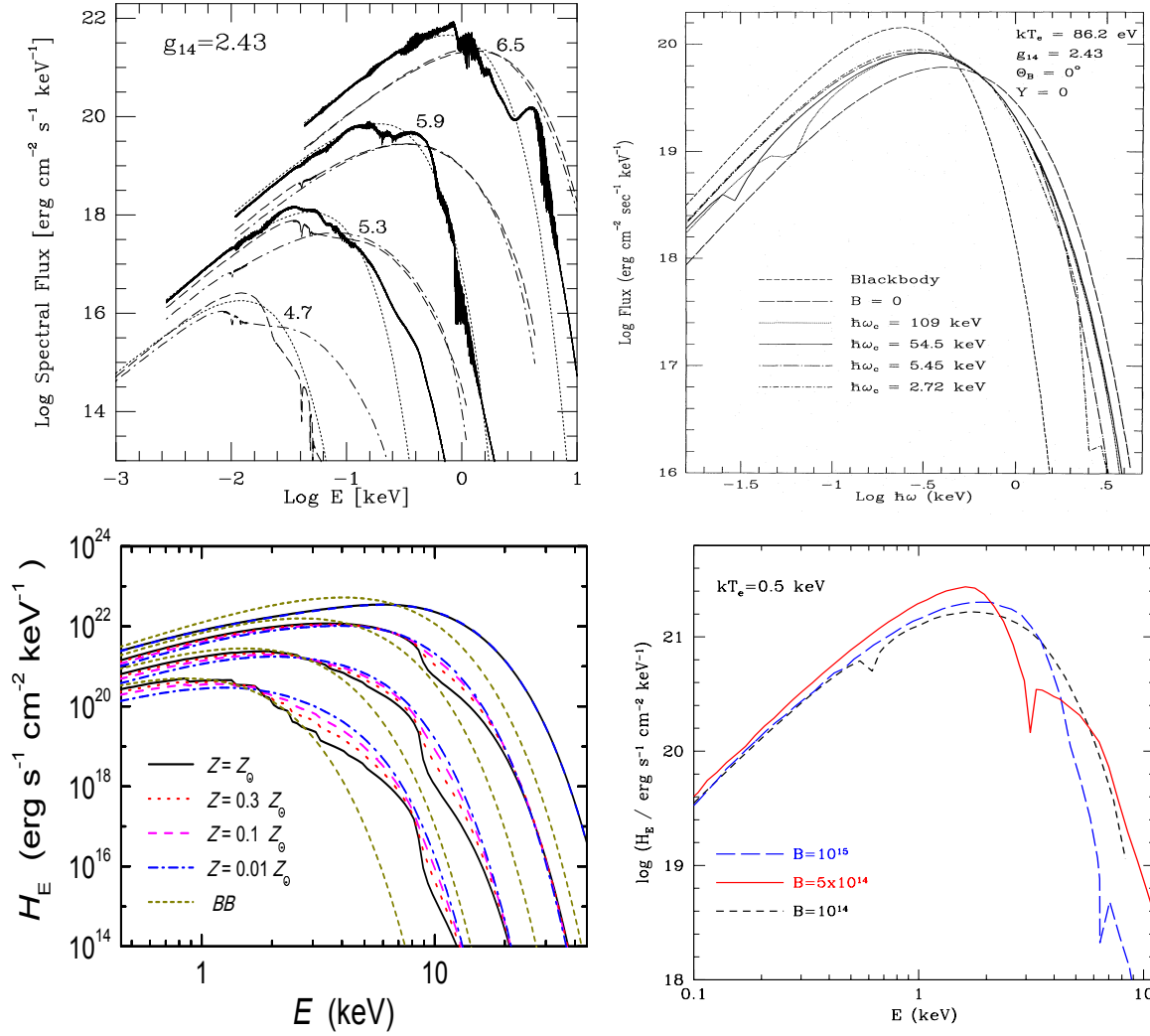


**Figure 3.** Model spectra for four different types of neutron stars. In all panels, the emerging flux is shown against photon energy in keV. The Eddington flux  $H_E$  is related to the spectral flux  $F_E$  by  $F_E = 4\pi H_E$ . A range of results are shown for different compositions, magnetic field strengths, and effective temperatures (labeled in K or eV =  $1.16 \times 10^4$  K). (*Top Left*) non-magnetic, cool neutron stars; each group of curves correspond to a different effective temperature ( $T_{\text{eff}} = 10^{4.7-6.5}$  K) with a range of compositions: dash-dotted lines represent H, dashed lines represent He, and solid lines represent Fe. Dotted lines show the blackbody at the effective temperature (Zavlin et al. 1996) (*Top Right*) cool neutron stars with moderate magnetic field strengths ( $B = 2 \times 10^{11} - 10^{13}$  G) and hydrogen composition, for an effective temperature  $T_{\text{eff}} = 86.2$  eV (Shibanov et al. 1992) (*Bottom Left*) hot bursting neutron stars with a range of metallicities as shown with different line styles and colors; each group of curves corresponds to a different effective temperature (Suleimanov et al. 2011) (*Bottom Right*) strongly magnetic neutron stars for a hydrogen compositions and different magnetic field strengths (Özel 2003). In all cases, the spectra show significant deviations from the blackbodies at the corresponding effective temperatures.

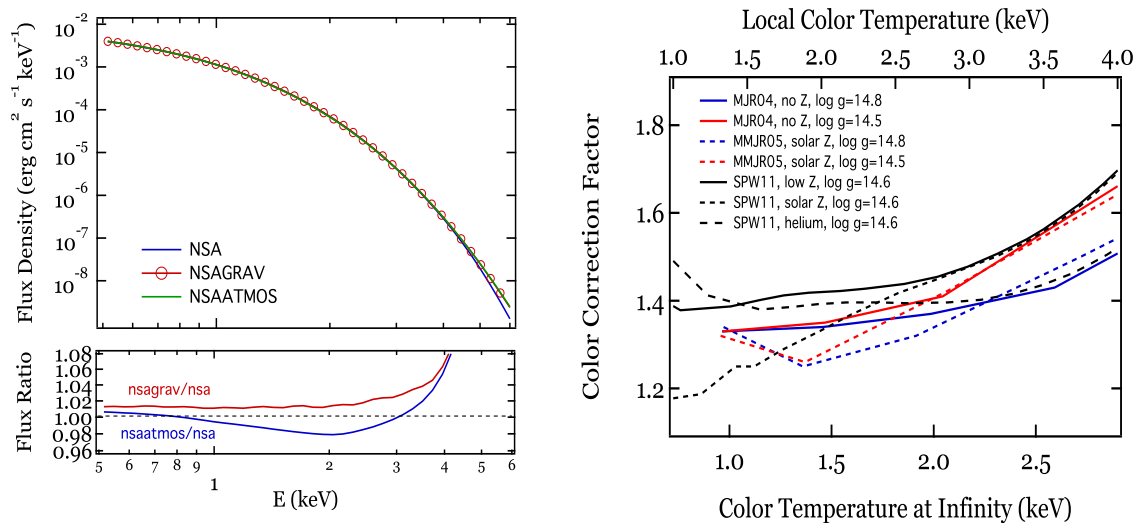


**Figure 4.** (*Left*) A comparison between three different non-magnetic neutron star atmosphere models computed for  $T_{\text{eff}} = 120$  eV. The three models shown are NSA, NSGRAV (Zavlin et al. 1996), and NSATMOS (Heinke et al. 2006). (*Right*) A comparison between the color correction factors obtained for atmosphere models for accreting bursting neutron stars for different effective temperatures, surface gravities, and atmospheric compositions. The models shown are from Madej et al. 2004 (MJR04), Majczyna et al. 2005 (MMJR05), and Suleimanov et al. 2011 (SPW11). Different model calculations for the same input model parameters generate predictions that agree with each other at the 2-7% level.

these variations in technique and the treatment of processes, different model calculations may produce spectra that deviate from each other when computed for the same effective temperature, magnetic field strength, and surface composition.

As an example, Figure 4 shows a comparison of three different non-magnetic hydrogen atmosphere models computed for  $T_{\text{eff}} = 120$  eV, for a neutron star with a radius of 10 km and a  $1.4 M_{\odot}$  mass, assuming no interstellar extinction. All three models are available on the spectral analysis software XSPEC under the names NSA, NSGRAV (Zavlin et al. 1996), and NSATMOS (Heinke et al. 2006) and are widely used to fit the observed spectra of neutron stars. The lower panel shows the fractional differences between the models, which are most evident at the high energy tail. In general, however, these model calculations generate predictions that are consistent at the 2-6% level, depending on the photon energy.

As a second example, Figure 4 shows the color correction factors obtained for atmosphere models of bursting neutron stars for different effective temperatures and atmospheric compositions based on calculations of different groups (MJR04: Madej et al. 2004; MMJR05: Majczyna et al. 2005; SPW11: Suleimanov et al. 2011). These models are, on average, hotter than those shown in the left panel, and the spectral shapes are dominated by the effects of Compton scattering. The color correction factors shown in the figure provide only a gross characterization of the spectral shapes and

the actual values depend on the technique used to calculate them (see Suleimanov et al. 2011 for a discussion). Nevertheless, the dependence of the color correction factors on the physical conditions and on the particular numerical techniques is weak and the differences are limited to  $\lesssim 7\%$ .

Absorption features in the spectra result from bound-free atomic transitions, cyclotron absorption, or vacuum polarization. As expected, at higher metallicities and at lower temperatures, where higher fraction of neutrals may be present, there are large numbers of bound-free absorption lines. Light elements such as hydrogen and helium can also give rise to spectral features at low effective temperatures, especially at high magnetic field strengths ( $B \gtrsim 10^{12}$  G), where their ionization energies are significantly higher than in the non-magnetic case.

In the presence of strong magnetic fields, electron or proton cyclotron features also appear in neutron star surface spectra. When the field strength is in the  $10^{11-12}$  G range, the electron cyclotron energy falls in the soft X-ray band, while in the  $10^{14-15}$  G range, it is the protons that produce the absorption features in the spectra. Proton cyclotron features at different magnetic field strengths are shown in the lower right panel of Figure 3. At these strong fields, vacuum polarization resonance also plays an important role in shaping the neutron star surface spectra and affects the features in two ways. First, the conversion of photon polarization modes as they propagate outward to lower plasma densities and the enhanced interaction cross sections associated with this resonant conversion give rise to very broad absorption features in the tail of the spectra and reduce the overall hardening. Second, vacuum polarization dramatically suppresses the equivalent widths of cyclotron lines (Özel 2003; Ho & Lai 2003; see Figure 3).

There are a number of mechanisms that determine the widths of atomic features in the thermal spectra of neutron stars. Pressure broadening due to the Stark effect is caused by the shifting and splitting of atomic lines from an atom in the presence of the static electric fields from the neighboring ions. Considering the first-order effect that is linear in the electric field, Paerels (1997) and Chang, Bildsten, & Wasserman (2005) estimated the amount of broadening due to this effect as

$$\Delta E_{\text{Stark}} \simeq \frac{\hbar^2 n^2}{m_e Z r_0^2} \simeq 1.5 \left(\frac{Z}{26}\right)^{-1} \left(\frac{n_i}{10^{23} \text{ cm}^{-3}}\right)^{2/3} \left(\frac{n}{3}\right)^2 \text{ eV}, \quad (26)$$

where  $Z$  is the atomic number of the atom,  $r_0$  is the mean ion spacing,  $n_i$  is the number density of ions, and  $n$  is the principal quantum number of the upper level of the transition. This can be compared to the thermal Doppler broadening

$$\Delta E_D = \left(\frac{2k_B T}{A m_p c^2}\right)^{1/2} E_0 \simeq 0.20 \left(\frac{k_B T}{1 \text{ keV}}\right)^{1/2} \left(\frac{A}{56}\right)^{-1/2} \left(\frac{E_0}{1 \text{ keV}}\right) \text{ eV}, \quad (27)$$

where  $A$  is the mass number of the atom and  $E_0$  is the energy of the transition. For rapidly spinning neutron stars, both of these effects can be negligible compared to rotational broadening (Özel & Psaltis 2003; Chang et al. 2006), which has a characteristic scale of

$$\Delta E_{\text{rot}} = \frac{4\pi \nu_s R}{c} E_0 \simeq 240 \left(\frac{\nu_s}{600 \text{ Hz}}\right) \left(\frac{R}{10 \text{ km}}\right) \left(\frac{E_0}{1 \text{ keV}}\right) \text{ eV}, \quad (28)$$

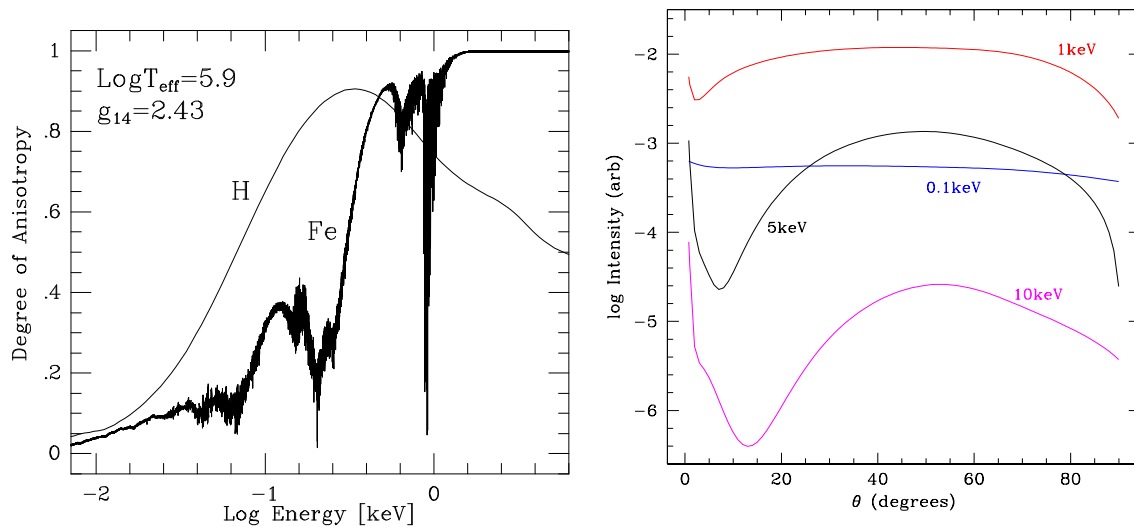


**Figure 5.** (*Left*) The beaming of radiation emerging from the surface of a non-magnetic neutron star for different atmospheric compositions (Zavlin et al. 1996). The degree of anisotropy is defined in equation (30) in the text. The complex structure of the degree of anisotropy in the iron atmosphere reflects the strong and non-monotonic energy dependence of the interaction cross sections, which causes a variable degree of limb darkening as a function of photon energy. (*Right*) The beaming of radiation emerging from the surface of a  $10^{14}$  G magnetar at four different photon energies (Özel 2001). The characteristic “pencil” and “fan” components are visible, especially at the higher photon energies.

where  $\nu_s$  is the spin frequency of the neutron star. Finally, in the presence of a magnetic field, Zeeman splitting of the atomic levels is responsible for additional broadening with a scale given by (see Loeb 2003)

$$\Delta E_Z \simeq \left( \frac{e\hbar}{m_e c} \right) (M_L + 2M_S) B \simeq 5.8(M_L + 2M_S) \left( \frac{B}{10^9 \text{ G}} \right) \text{ eV}, \quad (29)$$

where  $M_L$  and  $M_S$  are the quantum numbers of the orbital angular momentum and the spin of the electron.

### Angular Distribution (Beaming) of the Surface Emission

Various physical phenomena render the intensity of radiation emerging from the neutron star surface anisotropic. The large temperature gradient in the atmosphere, in combination with energy dependent cross sections for the interactions between the photons and matter, scattering processes, as well as the presence of a strong magnetic field can cause this anisotropy, also referred to as beaming. Figure 5 shows the beaming of emission from a non-magnetic and a strongly magnetic isolated neutron star. For the non-magnetic case, the degree of anisotropy, defined as

$$a_\nu = \frac{I_\nu(\mu = 1) - I_\nu(\mu = 0)}{I_\nu(\mu = 1) + I_\nu(\mu = 0)} \quad (30)$$

is plotted against the photon energy for two compositions of the atmosphere (Zavlin et al. 1996). Here,  $\mu$  is the cosine of the angle between the photon direction of propagation and the surface normal and  $I_\nu(\mu = 1)$  and  $I_\nu(\mu = 0)$  are the frequency-dependent intensities of the emerging radiation along and perpendicular to the surface normal, respectively. The complex structure of the degree of anisotropy in the iron atmosphere reflects the strong and non-monotonic energy dependence of the interaction cross sections, which causes a variable degree of limb darkening as a function of photon energy.

In the strongly magnetic atmosphere case, the figure shows the angular dependence of the emerging radiation for four different photon energies (Özel 2001). The beaming is characterized by the presence of a narrow “pencil” component, along the magnetic field direction, as well as a broad “fan” component, at large angles from the field direction (see Meszaros 1992). The orientations with the highest intensity in the two components correspond to the directions of propagation with the reduced opacities for the two normal modes of polarization.

The anisotropy of radiation emitted from neutron star surfaces has a direct effect on the observed properties of spinning neutron stars: it alters the broadening of the spectrum and the amplitude of the pulsations due to general relativistic effects, which are discussed below.

#### 2.4. Observed Physical Quantities

The observational appearance of a neutron star is affected by its spacetime, since photons that originate from the neutron star surface get redshifted and lensed as they propagate to a distant observer. Even though the combined effects of redshift and lensing, in general, can only be calculated numerically (see Pechenick, Ftaclas, & Cohen 1983), several observable properties of a slowly spinning neutron star that is emitting uniformly depend only on a single element of its metric,  $g_{tt}$ , evaluated on its surface (Psaltis 2008). This is true for any general metric theory of gravity. In particular, in the Schwarzschild geometry, the time-time component of the metric is given by  $g_{tt} = -(1 - 2GM/Rc^2)$ , where  $M$  and  $R$  are the mass and the coordinate radius of the neutron star, respectively. As a result, the gravitational effects on the observational appearance of a slowly spinning neutron star can be characterized by the single parameter  $p \equiv 2GM/Rc^2$ , which is often called the compactness. For different equations of state of neutron-star matter, the predicted compactness of a neutron star ranges from  $\sim 0.25$  to  $\sim 0.65$ , with the higher values corresponding to the stars that are more massive and smaller in size.

Photons that propagate from the surface of a slowly spinning neutron star to a distant observer are gravitationally redshifted by an amount

$$1 + z = |g_{tt}|^{-1/2} = \left(1 - \frac{2GM}{Rc^2}\right)^{-1/2}. \quad (31)$$

At the same time, they are lensed by the strong gravitational field of the neutron star, causing its apparent area at infinity to appear larger by an amount equal to (see Psaltis,

Özel, & DeDeo 2000)

$$\frac{S_\infty}{4\pi R^2} = (1+z)^2 = \left(1 - \frac{2GM}{Rc^2}\right)^{-1}, \quad (32)$$

and its apparent radius to appear larger by

$$R_{\text{app}} = R \left(1 - \frac{2GM}{Rc^2}\right)^{-1/2}. \quad (33)$$

If we denote by  $T_{\text{eff},s}$  the effective temperature of radiation on the neutron star surface, then the effective temperature measured by a distant observer is also redshifted, i.e.,

$$T_{\text{eff},\infty} = \frac{T_{\text{eff},s}}{1+z} \quad (34)$$

so that the total flux observed from the neutron star at a large distance  $D$  becomes

$$F_\infty = \sigma_B T_{\text{eff},\infty}^4 \left(\frac{R}{D}\right)^2 (1+z)^2 = \sigma_B T_{\text{eff},\infty}^4 \left(\frac{R}{D}\right)^2 \left(1 - \frac{2GM}{Rc^2}\right)^{-1}. \quad (35)$$

Finally, the Eddington luminosity at infinity is also affected by both the redshift and the gravitational lensing of the photons and is equal to

$$L_{\text{E},\infty} = \frac{8\pi m_p c}{(1+X)\sigma_T} R^2 g_{\text{eff}} (1+z)^{-2}, \quad (36)$$

where,  $g_{\text{eff}}$  is the effective gravitational acceleration on the neutron star surface. In general relativity,  $g_{\text{eff}} = (1+z)GM/R^2$  and the Eddington luminosity becomes

$$L_{\text{E},\infty} = \frac{8\pi GM m_p c}{(1+X)\sigma_T} \left(1 - \frac{2GM}{Rc^2}\right)^{1/2}. \quad (37)$$

Increasing the spin of a neutron star affects its observable properties in at least three ways. First, Doppler boosting of the emission makes the apparent image of the neutron star asymmetric, with the approaching side appearing brighter than the receding side, and broadens any spectral features that originate on its surface. Second, frame dragging alters the propagation of photons in the neutron star spacetime and contributes to enhancing the asymmetry of emission. Finally, as the spin frequency of a neutron star approaches the breakup frequency, the star becomes significantly oblate. Several authors have explored, at different levels of approximation, the effects of increasing the spin of a neutron star on several observables such as the lightcurves that arise when the surface emission on a spinning neutron star is not uniform (Miller & Lamb 1998; Braje, Romani & Rauch 2000; Muno, Özel & Chakrabarty 2003; Poutanen & Gierlinski 2003; Cadeau, Leahy & Morsink 2005; Cadeau et al. 2007; Morsink et al. 2007), the rotational broadening of atomic lines that originate on the stellar surfaces (Özel & Psaltis 2003; Bhattacharyya, Miller & Lamb 2006; Chang et al. 2006), as well as their apparent surface areas (Bauböck et al. 2012).



**Table 1.** Categories of Neutron Stars with Surface Emission

Source Type	Other Names <sup>a</sup>	Age (yr)	Temp. (10 <sup>6</sup> K)	Mag. Field (G)	Companion?	Pulsations?
Quiescent Accreting NS	qLMXB	$\gtrsim 10^9$	0.6 – 2	$\leq 10^9$	Y	N
Bursts	LMXB	$\gtrsim 10^9$	10 – 35	$\leq 10^9$	Y	S <sup>b</sup>
Accreting msec Pulsars	AMSP	$\gtrsim 10^9$	5 – 10	$10^{8-9}$	Y	Y
Rotation Powered MSP	MSP	$\sim 10^{9-10}$	2 – 8	$10^{8-9}$	S	Y
Isolated Cooling NS	PSR	$10^{3-5.5}$	0.6 – 2	$10^{11-12}$	N	Y
–”–	DINS, CCO	$10^{5.5-6.6}$	0.6 – 1.3	?	N	S
Magnetars	AXP, SGR	$10^{5.5-6.6}$	3 – 8	$10^{14-15}$	N	Y

Notes: (a) Typical related acronyms often used in the literature for these categories; qLMXB: quiescent low-mass X-ray binaries, LMXB: low-mass X-ray binaries, AMSP: accretion powered millisecond pulsars, MSP: millisecond pulsars, PSR: pulsating sources in the radio, DINS: dim isolated neutron stars, CCO: central compact objects, AXP: anomalous X-ray pulsars, SGR: soft gamma-ray repeaters. (b) S: sometimes.

### 3. A Census of Neutron Star Sources with Surface Emission

Surface emission has been detected from a large variety of neutron star sources to date. The spectra of this emission are thermal or have a distinguishable thermal component that peaks at wavelengths from the optical regime to the X-rays. The sources include isolated neutron stars and accreting neutron stars in binaries with ages ranging from hundreds to billions of years, as summarized in Table 1. In this section, I will discuss the properties of the sources that show emission from their surfaces.

#### 3.1. Accreting Neutron Stars in Quiescence

About half of known neutron stars accreting from a low-mass companion star manifest themselves as X-ray transients (see Liu et al. 2007). X-ray transients experience several different recurrent accretion phases, from quiescence to outburst, which are distinguished by varying flux levels and spectral characteristics. The outburst luminosities of these accreting neutron stars are typically  $10^{36-38}$  erg s<sup>-1</sup>, compared to their quiescent luminosities, which are of the order  $10^{36-38}$  erg s<sup>-1</sup>. At the high mass accretion rates during the outbursts that last  $\sim$  months, the emission is dominated by the accretion disk. On the other hand, during quiescence when mass accretion onto the neutron star either ceases or continues at very low levels, the observed X-ray emission originates primarily from the neutron star surface. Other general properties of this class of sources is shown in Table 1.

The launch of X-ray telescopes with good spatial and energy resolution and low background, such as the Chandra X-ray Observatory and XMM-Newton, have enabled detailed studies of these sources. About a dozen neutron star X-ray transient systems have been detected in quiescence as well as in outburst. There is, by now, strong evidence that the quiescent emission of neutron star sources is brighter by more than

**Table 2.** Accreting Neutron Stars in Quiescence

Name	Temperature $\log(T/\text{K})$	Distance (kpc)	Luminosity <sup>a</sup> ( $10^{32} \text{ erg s}^{-1}$ )	References <sup>b</sup>
NS in $\omega$ Cen	6.0	5.3	4.9	1
NS in M13	6.0	7.7	5.1	1
NS in NGC 2808	6.0	9.6	10.0	1
U24 in NGC 6397	6.0	2.5	1.1	2
X7 in 47 Tucanae	6.1-6.2	4.9	15.0	3
KS 1731–260	6.08–5.86	7.0 <sup>c</sup>	24-4	4, 5
MXB 1659–29	6.15–5.80	10.0 <sup>c</sup>	49-2	4, 6
XTE J1701–462	6.28–6.15	8.8 <sup>c</sup>	166-50	7
EXO 0748–676	6.15–6.1	7.4 <sup>c</sup>	100-60	8

Notes: (a) The unabsorbed bolometric luminosity of the thermal component of the observed emission. (b) References. 1. Webb & Barret 2007; 2. Guillot et al. 2011; 3. Heinke et al. 2006; 4. Cackett et al. 2006; 5. Cackett et al. 2010; 6. Cackett et al. 2008; 7. Fridriksson et al. 2011; 8. Degenaar et al. 2011. (c) Approximate distances.

an order of magnitude than the quiescent emission of black hole transients in similar binary systems (Garcia et al. 2001), pointing to the role of the neutron star surface in producing the quiescent emission. Numerous observations during quiescent periods also revealed that there is a soft thermal component in the X-ray spectra, characterized by blackbody temperatures of 0.1 – 0.3 keV, in a fraction of sources (see Figure 6 and Table 2). This indicates that some of the accretion energy may be deposited as heat in the stellar interior during the accretion phases and reradiated from the surface during quiescence (Brown et al. 1998; see Section 2.1). However, there have also been numerous detections of non-thermal X-ray emission, typically described by a power-law component above  $\sim$  few keV, as well as of variability in the flux levels during quiescent episodes. These strongly suggest that at least a fraction of the emission arises from continued accretion (Garcia et al. 2001) or coronal emission from the companion star (Bildsten & Rutledge 2000; Campana & Stella 2000). Changing crust properties of the neutron stars leading to time variability has also been discussed as an alternative (see, e.g., Cackett et al. 2010b).

Observations of neutron stars in quiescence have been geared towards: (i) obtaining the apparent radii of neutron stars by fitting their spectra with detailed atmosphere models and (ii) inferring the properties of the neutron star crust and core by tracking their flux and temperature evolution during quiescence (see the right panel of Figure 6). Table 2 summarizes the observations of sources which have been used in spectral and cooling studies in order to measure the neutron star radius or to infer the properties of their crusts and cores.

Other transient sources that have been monitored over long periods of time and studied spectroscopically include Cen X–4 (Cackett et al. 2010b), Aql X–1 (Cackett et al. 2011), 4U 1608–522 (Rutledge et al. 1999; Wachter et al. 2002), EXO 1745–248

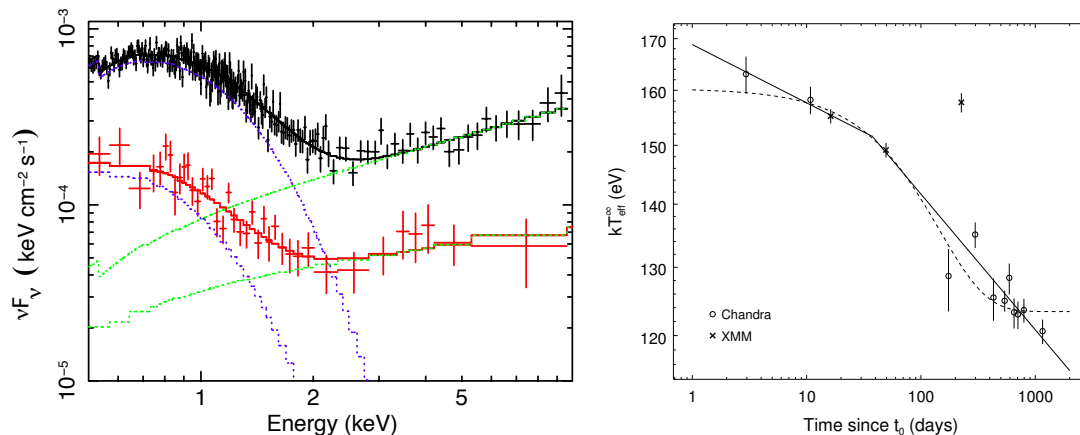


**Figure 6.** (*Left*) The spectrum of Cen X-4 at two different quiescent epochs (Cackett et al. 2010b). The spectra demonstrate two frequently observed properties of neutron star transients in quiescence: (*i*) the presence of a thermal component (shown as blue dashed curves) as well as a power-law component (green dotted line, here dominant above  $\sim 2$  keV). (*ii*) the variability in the flux between different quiescent epochs. The black spectrum shows the brightest and red the faintest quiescent observations of Cen X-4. The spectra have been rebinned for visual clarity. (*Right*) The effective neutron star surface temperature of XTE J1701–462 during quiescence, with best-fit cooling curves shown (Fridriksson et al. 2011). The curves correspond to different fits of the observed cooling trend.

(Degenaar & Wijnands 2012), and RX J170930.2–263927 (Jonker et al. 2003). The majority of these sources show variability in their quiescent flux, pointing to a low level of continued accretion. The ratio between their quiescent luminosity and accretion luminosity has been inferred through long-term averages and used to place constraints on the storage efficiencies in the cores of these neutron stars (see Section 5).

A number of accretion powered millisecond pulsars, which are also X-ray transients, have been observed in quiescence. In the case of SAX J1808.4–3658 and XTE J1751–305, the quiescent spectra are non-thermal, with a possible contribution from a thermal component limited to  $< 30$  eV and  $< 71$  eV, respectively (Campana et al. 2002; Heinke et al. 2009). The quiescent flux of IGR J00291+5934, observed at multiple epochs with Chandra and XMM-Newton, shows some variability. Its spectrum is hard and, as in the case of other quiescent millisecond pulsars, can be modeled by a power-law (Jonker et al. 2005), with a possible contribution from a thermal component at 64 eV (Campana et al. 2008). Note that while their quiescent properties are summarized here, accretion powered millisecond pulsars are discussed in more detail in section 3.3.

### 3.2. Accreting Bursting Neutron Stars

Approximately hundred out of  $\sim 150$  neutron stars accreting from low-mass companions have been observed to exhibit thermonuclear bursts, which manifest themselves as a

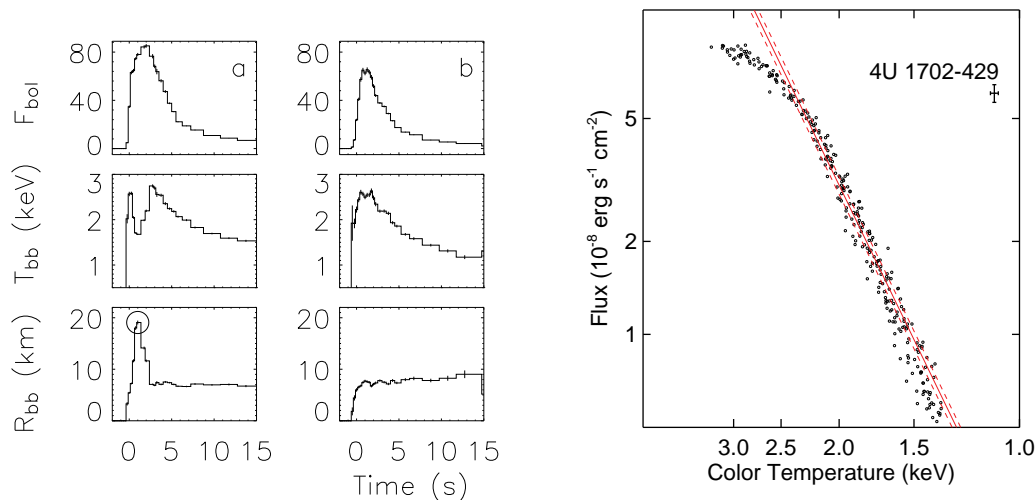


**Figure 7.** (Left) A thermonuclear burst from 4U 1636+536 showing a photospheric radius expansion burst in panel (a) compared to an ordinary burst in panel (b). The three panels shown for each burst are the bolometric flux in units of  $10^{-9}$  erg s $^{-1}$  cm $^{-2}$ , the blackbody temperature, and the radius of the blackbody assuming that the source lies at 6 kpc (Galloway et al. 2006). (Right) The flux-temperature diagram for the bursts from 4U 1702–429 observed with the RXTE (Güver et al. 2012b). The diagonal lines show the best fit blackbody normalization and its uncertainty. This figure shows that the apparent surface areas during the cooling tails of many X-ray bursts are highly reproducible.

sudden rise in the X-ray flux that lasts  $\sim 10 - 100$  s, accompanied by a characteristic evolution of the inferred temperature, as shown in Figure 7 (see Galloway et al. 2008 for a catalog of burst observations). The bursts are caused by the unstable burning of the helium layer (sometimes mixed with hydrogen) accreted onto the neutron star surface (see Section 2.1).

Even though their discovery dates back to 1975 (Grindlay et al. 1976; Belian, Conner, & Evans 1976), the study and the statistics of thermonuclear burst sources have improved greatly with the Rossi X-ray Timing Explorer (RXTE) in the past decade, which observed well in excess of 1000 burst events. Spectral studies at high time resolution revealed thermal spectra throughout each burst (Swank et al. 1977; Galloway et al. 2008; Güver et al. 2012b), with blackbody temperatures that reach 2 – 3 keV at the burst peak. The angular size corresponding to the emitting area on the neutron star surface is obtained by

$$\frac{R}{D} = \left( \frac{F_{\text{bol}}}{\sigma_{\text{B}} T_{\text{BB}}^4} \right)^{1/2}, \quad (38)$$

where  $D$  is the distance to the star, the color temperature  $T_{\text{BB}}$  is inferred from fitting blackbody functions to the spectra, and  $F_{\text{bol}}$  is the observed bolometric flux. (Note that this angular size needs to be corrected by the color correction factor for atmospheric effects, see Equation [25]). The angular size shows a rapid increase in the burst rise

(see Figure 7; Strohmayer, Zhang, & Swank 1997), as the burst spreads throughout the neutron star surface, and remains nearly constant during the burst decay, also referred to as the cooling tail. A statistical study of the cooling tails of bursters that showed multiple bursts in the RXTE database revealed remarkable consistency in the angular size obtained from different bursts of the same source (Güver et al. 2012b). An example of a flux-temperature diagram with a highly reproducible angular size is shown in the right panel of Figure 7. The angular sizes of the bursting neutron stars included in that study are given in Table 3.

A subset of bright bursts shows a particular evolution of the color temperature and the angular size throughout the burst, where a dip in the temperature accompanies a rise of the photospheric radius to values that are significantly larger than the angular size observed in the cooling tail (Lewin, van Paradijs, & Taam 1993). The two examples in the left panel of Figure 7 compare such a burst with an ordinary one. In these photospheric radius expansion episodes, the burst flux reaches the local Eddington limit and provides a measure of this quantity for each source (Paczynski 1983; Kato 1983). For sources that show repeated photospheric radius expansion bursts, the uncertainties in the Eddington limit can be quantified (Damen et al. 1990; Kuulkers et al. 2003; Güver et al. 2012a). Table 3 shows the bolometric Eddington flux corrected for interstellar extinction for bursters that have been reported to have two or more photospheric radius expansion episodes in the catalog of Galloway et al. (2008). The Eddington limit measured in bursts have been used as distance indicators (Kuulkers et al. 2003) as well as for measuring the properties of the neutron star (van Paradijs 1978, 1979; Damen et al. 1990; Özel et al. 2009).

Periodic flux oscillations have been observed in both the rise and the cooling phases of thermonuclear bursts (Strohmayer et al. 1996; Galloway et al. 2008). In the burst rise, spreading of the burning front in the accreted layer is modulated at the neutron star spin period, causing a periodic signal (Strohmayer et al. 1997). In the cooling phases, modes excited on the neutron star surface are thought to give rise to burst oscillations (Muno et al. 2002, 2003; Heyl 2004; Piro & Bildsten 2005; Narayan & Cooper 2007). Burst oscillations have been used to measure the spin period of neutron stars (Chakrabarty et al. 2004). Moreover, the shapes and amplitudes of the pulses occurring on the neutron star surface have been used to measure the stellar gravity, as will be discussed in Section 4.2.

### *3.3. Accreting Millisecond X-ray Pulsars*

Neutron stars accreting steadily over a long period of time from a low-mass companion are believed to have their surface magnetic fields reduced from  $\sim 10^{12}$  G to  $\sim 10^8$  G and their spin periods reduced to milliseconds by accretion torques (Alpar et al. 1982; Radhakrishnan & Srinivasan 1982). Observations with RXTE revealed persistent millisecond pulsations in the X-ray flux from a number of sources (Wijnands & van der Klis 1998), confirming this expectation. The known sources belonging to this

**Table 3.** Neutron Stars with Thermonuclear Bursts

Name	Angular Size (km/10 kpc)	Eddington Flux ( $10^{-8}$ erg s $^{-1}$ cm $^{-2}$ )	Distance (kpc)	References <sup>a</sup>
4U 1608–52	18.0±0.1	15.4±0.65	5.8 $^{+2.0}_{-1.9}$	1
4U 1636–53	11.4±1.0	6.93±0.64	—	2,3
4U 1702–429	13.3±0.4	—	—	2,3
4U 1705–44	9.2±0.5	—	—	2,3
4U 1724–307	10.7±0.7	5.29±0.70	—	2,3
4U 1728–34	11.6±0.7	8.63±0.46	—	2,3
KS 1731–260	9.8±0.4	4.71±0.13	5–11	2,3,4
4U 1735–44	8.5 $^{+0.08}_{-0.06}$	3.15±0.11	—	2,3
EXO 1745–248	10.8±1.2	6.25±0.2	6.3±0.6	5
4U 1746–37	4.0±0.3	—	—	2,3
SAX J1748.9–2021	9.5±0.5	4.03±0.54	—	2,3
SAX J1750.8–2900	9.6±0.5	5.61±0.17	—	2,3
4U 1820–30	9.6±0.1	5.39±0.12	6.8–9.6	6
GS 1826–24	10.2±0.03	—	—	7
Aql X–1	—	10.44±0.22	—	3

Notes: References. (a) 1. Güver et al. 2010a; 2. Güver et al. 2012a; 3. Güver et al. 2012b; 4. Özel et al. 2012; 5. Özel et al. 2009; 6. Güver et al. 2010b; 7. Galloway & Lampe 2012.

category are shown in Table 4. Note that there is some overlap between this category and the previous two categories (see Table 1), as all accreting millisecond pulsars are transients (Section 3.1), some of which have been followed into quiescence, and some show thermonuclear X-ray bursts (Section 3.2).

Among the sources that have shown thermonuclear X-ray bursts, there have been detections of burst oscillations in six of them. The asymptotic burst oscillation frequency is very similar to the frequency of persistent pulsations, providing strong evidence that both frequencies are equal to the spin frequency of the neutron star (Chakrabarty et al. 2003).

The pulsed X-ray emission from millisecond pulsars is thought to originate from the footpoints of the accretion column onto the polar cap of the neutron star. The spectrum and the angular distribution of emission in this case is not well understood. It requires modeling of both the thermal emission from the boundary layer where the accretion column is stopped at the neutron star surface as well as of the reprocessing of this radiation through the accretion column. Simplifying assumptions about the geometry and the temperature/density structure of the polar cap region and the accretion column have often been employed (see, e.g., Poutanen & Gierlinski 2003; Leahy, Morsink, & Cadeau 2008). Even though the observed spectra do not appear to have a dominant blackbody component, the Comptonization of the surface blackbody photons in the accretion column is believed to generate the power-law spectra that are observed up to  $\sim 100$  keV (see Poutanen & Gierlinski 2003). The angular distribution of the emerging radiation, in this model, is peaked along the radial direction, with a broad fan beam

**Table 4.** Millisecond X-ray Pulsars

Source Name	Spin Frequency (Hz)	Orbital Period (min)	Comments	References <sup>a</sup>
IGR J00291+5934	599	147		1
XTE J0929–314	185	43.6		2
NGC6440 X–2	206	57		3
SAX J1748.9–2021 <sup>b</sup>	442	522		4
Swift J1749.4–2807	518	529		5
IGR J1749.8–2921	11	1275.1	BO <sup>c</sup>	6
XTE J1751–305	435	42.4		7
IGR J1751–30.57	245	208	BO	8
SWIFT J1756.9–2508	182	54.7		9
XTE J1807–294	191	40.1		10
SAX J1808.4–3658	401	121	BO	11
XTE J1814–338	314	257	BO	12
HETE J1900.1–2455 <sup>b</sup>	377	83.3	BO	13
Aql X-1 <sup>b</sup>	550	1194	BO	14

Notes: (a) References. (1) Galloway et al. 2005; (2) Galloway et al. 2002; (3) Altamirano et al. 2010a; (4) Patruno et al. 2009; (5) Altamirano et al. 2011; (6) Altamirano et al. 2010b; (7) Markwardt et al. 2002; (8) Papitto et al. 2011; (9) Krimm et al. 2007; (10) Kirsch et al. 2004; (11) Wijnands & van der Klis 1998; (12) Watts et al. 2005; (13) Galloway et al. 2007; (14) Casella et al. 2008; (b) Intermittent pulsations; (c) Burst Oscillations observed.

component due to Comptonization.

The observed persistent pulsations have amplitudes in the 1–12% range (see Table 1 of Özel 2009), where the lower value reflects a typical sensitivity for short duration searches. (Deeper searches have been performed in a small number of persistent sources and yielded either upper limits below 1% or the discovery of small amplitude intermittent pulsations; see Dib et al. 2005 and Casella et al. 2008). As in the case of burst oscillations, the persistent pulsations have been used to constrain the masses and radii of neutron stars (see Section 4.2). The shape of the footpoint of the accretion column, where the thermal emission originates from, as well as its location with respect to the rotation axis, present challenges in modeling the pulse shapes. Indeed, there are theoretical calculations that point to non-circular footpoints (Bachetti et al. 2010) as well as observational evidence that the footpoints show long-term motions on the stellar surface (Papitto et al. 2007; Hartman et al. 2008).

### 3.4. Rotation-Powered Millisecond Pulsars with Thermal Emission

In the standard recycling paradigm (Alpar et al. 1982; Radhakrishnan & Srinivasan 1982), rotation-powered millisecond pulsars emerge as the descendants of accreting millisecond pulsars when accretion ceases. As in the case of other rotation-powered pulsars, these sources show predominantly non-thermal emission from their magnetospheres. However, recent X-ray studies have shown that a number of rotation-

powered millisecond pulsars also exhibit thermal soft X-ray emission (Grindlay et al. 2002; Zavlin 2006, 2007; Bogdanov et al. 2006a). Deep observations of globular clusters with Chandra and XMM-Newton have been particularly successful in identifying the presence and characteristics of the soft thermal emission from these sources (see, e.g., Becker et al. 2003; Webb, Olive, & Barret 2004; Bassa et al. 2004; Elsner et al. 2008; Bogdanov & Grindlay 2009; Bogdanov et al. 2010, 2011).

The thermal emission in these rotation-powered pulsars originates from the polar caps on the neutron star surface and is modulated at the spin frequency of the star. The polar caps are believed to be heated as a result of bombardment by the relativistic pairs traveling in the magnetosphere (Ruderman & Sutherland 1975; Arons 1981; Harding & Muslimov 2001). The energy from the relativistic charges is deposited deep in the atmosphere and, therefore, the spectrum of emerging radiation has all the typical characteristics of surface emission discussed in Section 2.3. A power-law component is also detected in the X-ray spectra of these sources and has been attributed (*i*) to Comptonization of the thermal spectrum by the particles in the magnetosphere, or (*ii*) to non-thermal emission by pairs in the magnetosphere or by particles in the pulsar wind nebula (see Bogdanov et al. 2006 for a discussion).

As in the case of pulsed surface emission from accreting millisecond pulsars, the pulse profiles and the energy spectrum of rotation-powered millisecond pulsars have been used to constrain the compactness of neutron stars (see Section 4.2 below).

### 3.5. Isolated Cooling Neutron Stars

Radiation from isolated neutron stars originates predominantly from non-thermal processes in the pulsar magnetosphere, which often dwarfs any emission from the neutron star surface. Nevertheless, in a small number of young-to-middle age pulsars, as well as in some nearby isolated neutron stars, a soft thermal component in the optical/X-ray spectra has been unequivocally detected. Earlier convincing results of this detection of surface emission came from ROSAT observations of isolated pulsars (see Ögelman 1995; Becker & Trümper 1997 for a summary of ROSAT results). Subsequently, the ensemble of such sources has been significantly increased through observations with modern instruments (see Page et al. 2009 for a discussion of the most recent observations; see also the reviews by van Kerkwijk & Kaplan 2007 and Mereghetti 2011a).

The sources in this category have been subclassified under several different names, based often on the method of detection, as also shown in Table 1. For example, young neutron stars in supernova remnants are often called central compact objects, isolated neutron stars with low fluxes are called dim isolated neutron stars, etc. Table 5 summarizes the properties of surface emission in these sources, divided into two major groups: sources that were known to be rotation-powered pulsars and sources that were discovered through their thermal emission. Sources with only upper limits on thermal emission are not included in this table.

In radio pulsars, thermal radiation from the surface is superimposed on the non-



**Table 5.** Isolated Neutron Stars with Thermal Emission

Name	Distance (kpc)	SD Age <sup>a</sup> log( <i>t</i> /yr)	Kin. Age <sup>b</sup> log( <i>t</i> /yr)	Temp. log( <i>T</i> /K)	Luminosity <sup>c</sup> log( <i>L</i> /erg s <sup>-1</sup> )	Refs. <sup>d</sup>
PSR B0538+2817	1.2	4.47	—	6.1 <sup>d</sup>	32.6–33.6	1
PSR B0633+1748 <sup>e</sup>	0.12–0.22	5.53	—	5.8 <sup>d</sup>	30.9–31.5	1
PSR B0656+14	0.26–0.32	5.04	—	5.7 <sup>d</sup>	32.2–33.0	1
PSR J0822–4247 <sup>e</sup>	1.9–2.5	3.90	3.6	6.2	33.9–34.0	1
PSR B0833–45 <sup>e</sup>	0.22–0.28	4.05	4.3	5.8	33.4–33.7	1
PSR B1055–52	0.5–1.5	5.43	—	5.9 <sup>d</sup>	32.1–33.2	1
PSR 1119–6127	~8.4	3.2	—	6.2	33.0–33.4	2,3
1E 1207–52	1.3–1.9	—	3.9	6.2 <sup>f</sup>	33.3–33.8	1
PSR B1706–44	1.8–3.2	4.24	—	5.8	31.8–32.9	1
PSR B2334+61	< 3.1	4.6	~4	5.8	31.7–32.7	3
RX J0420.0-5022	—	6.3	—	5.7 <sup>d,f</sup>	—	4,5
RX J0720.4-3125	0.27–0.53	6.2	5.8	5.6–6.0 <sup>f</sup>	31.3–32.5	6
RX J0806.4-4123	—	—	—	6.0 <sup>d,f</sup>	—	4
RX J1308.6+2127	—	6.2	5.7-6.1	6.0 <sup>d,f</sup>	—	7,8, 9
RX J1605.3+3249	—	—	5.7	6.0 <sup>d,f</sup>	—	10, 11
RX J1856.5-3754	0.12	6.6	5.6	5.8	31.6	12,13,14
RX J2143.0+0654	—	6.6	—	6.1	—	15, 16

Notes: (a) Spindown age; (b) Kinematic age; (c) The bolometric luminosity of the thermal component. (d) References. 1. Page et al. 2004; 2. Safi-Harb & Kumar 1998; 3. Page et al. 2009; 4. Haberl et al. 2004; 5. Kaplan & van Kerkwijk 2011; 6. Kaplan et al. 2002, 2003, 2007; 7. Haberl et al. 2003; 8. Airhart et al. 2008; 9. Motch et al. 2009; 10. van Kerkwijk et al. 2004; 11. Tetzlaff et al. 2012; 12. Walter et al. 2010; 13. van Kerkwijk & Kaplan 2008; 14. Drake et al. 2002; 15. Kaplan & van Kerkwijk 2009; 16. Zane et al. 2005; (d) Temperature obtained through blackbody fit; (e) Alternate names: PSR B0633+1748 = Geminga, PSR J0822–4247 = Puppis A, PSR B0833–45 = Vela; (f) broad absorption lines in the X-ray spectrum.

thermal magnetospheric emission and contributes a fraction of the flux that decreases with age between  $\sim 10^3$ – $10^6$  yr. Typical temperatures obtained from fitting blackbodies and/or hydrogen atmospheres range from  $5 \times 10^5$  –  $1.5 \times 10^6$  K (see Table 5), where the lower end reflects the sensitivity of the X-ray instruments as well as the effect of interstellar extinction.

In nearby isolated neutron stars, the emission appears to be predominantly from their surfaces. The spectra of sources that are studied through the deepest observations reveal the presence of multiple components. For example, the spectrum of RX J1856–3754 shown in Figure 8 has been modeled by a completely featureless blackbody in the X-rays (Drake et al. 2002) but the emission observed in the optical is higher than the extrapolation of the X-ray blackbody. Therefore, the broadband spectrum has been interpreted as the sum of two blackbodies with different temperatures originating from hot and cold regions on the neutron star (Pons et al. 2002; Braje & Romani 2002; see, however, Ho 2007 for a discussion of limitations of this interpretation and alternative models). On the other hand, the optical emission from several other

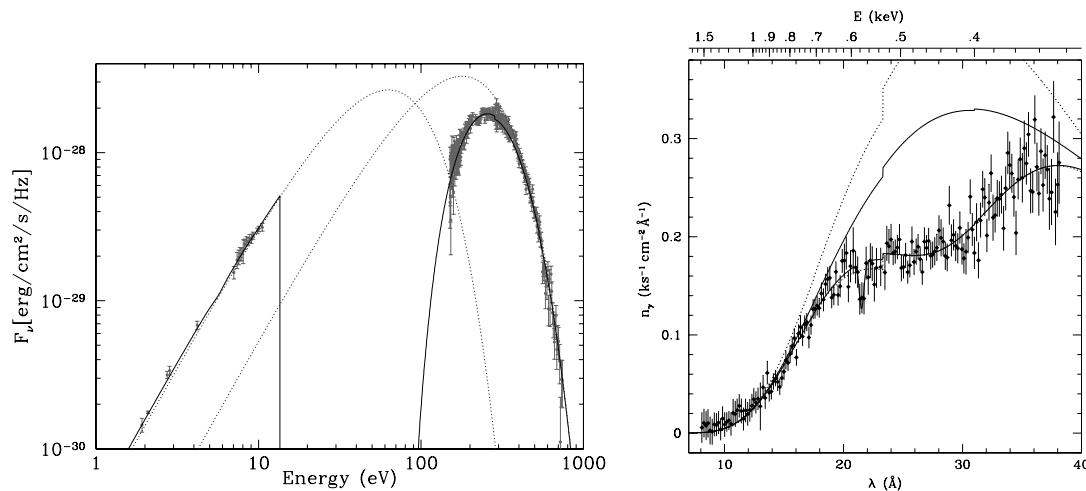


**Figure 8.** (*Left*) Broadband spectrum of RX J1856.5–3754 from Braje & Romani (2002) modeled with two blackbodies at  $kT = 61$  eV and  $kT = 20$  eV. (*Right*) A broad absorption feature observed in the spectrum RX J1605.3+3249 with RGS onboard XMM-Newton (van Kerkwijk et al. 2004). The two overplotted curves correspond to blackbodies with one (lower dotted line) and two (lower continuous line) Gaussian absorption features. Such features have been observed in the thermal spectra of several other nearby isolated neutron stars but have not been conclusively identified.

neutron stars, which has been studied with the Hubble Space Telescope, is also higher than the extrapolation of the X-ray blackbody but has a spectral slope that is inconsistent with a Rayleigh-Jeans tail (Kaplan et al. 2011). Moreover, in several sources such as PSR 1E1207–52 and RX J1605+3249, broad spectral features are clearly visible in their X-ray spectra, as shown in Figure 8. The origin of these features is not well established. They have been interpreted as cyclotron features (Sanwal et al. 2002; see also Halpern & Gotthelf 2011) as well as atomic features (see, e.g., Hailey & Mori 2002; Mori & Hailey 2006). The feasibility and potential problems of each interpretation is discussed in detail in van Kerkwijk et al. (2007).

Distances to several of the nearby sources have been determined accurately either via parallax measurements or via their associations with supernova remnants (see Table 5). Combined with the spectroscopic measurement of their angular sizes, this information has led to measurements of the neutron star radii (see, e.g., Pons et al. 2002). The difficulty in these measurements arises from the presence of multi-temperature components of emission from the neutron star surface that are inferred either from the detection of pulsed emission or from spectral modeling. The systematic uncertainties in these studies can be significantly reduced by combining the spectral information with the amplitudes of pulsed emission (Psaltis, Özel, & DeDeo 2000; Drake et al. 2002; Braje & Romani 2002).

The ages of some of these isolated neutron stars can be inferred via their associations with supernova remnants, their kinematic properties, or their spindown rates (Table 5). In combination with the distance and spectroscopic measurements discussed above, the

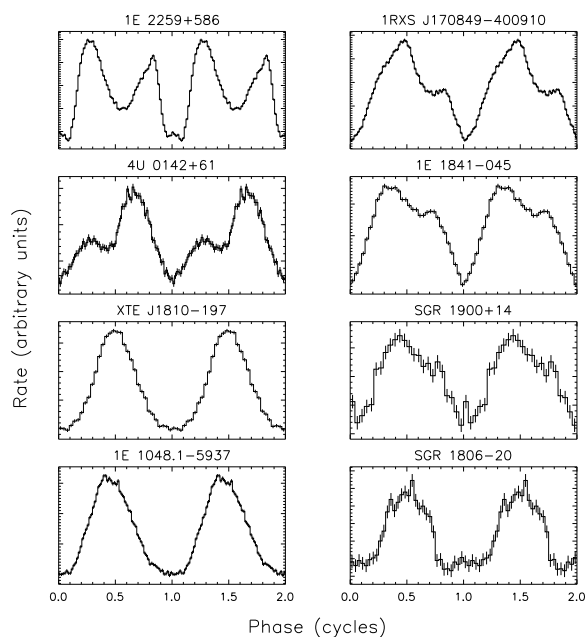


**Figure 9.** Pulse profiles of magnetars observed in the X-rays showing significant harmonic structure (Woods & Thompson 2004 using data from F. Gavriil and V. Kaspi.)

time evolution of the X-ray luminosity from these sources can be studied. As it will be discussed in Section 5, this provides one of the best tools for probing the cooling and, hence, the interior composition, of neutron stars.

### 3.6. Anomalous X-ray Pulsars and Soft Gamma Ray Repeaters

One last class of neutron stars from which surface emission has been observed includes the isolated sources referred to as Anomalous X-ray Pulsars (AXPs) and Soft Gamma-ray Repeaters (SGRs). These X-ray sources have persistent luminosities of  $10^{34-36}$  erg s $^{-1}$  and temperatures in the range  $kT \sim 0.3 - 0.6$  keV. They all show pulsed X-ray emission, from which their spin periods and period derivatives can be measured. The high observed spindown rates,  $\dot{P} \sim 10^{-11}$  s s $^{-1}$ , yield dipole magnetic field strengths in excess of  $10^{13}$  G (Kouveliotou et al. 1998; see Equation 7 as well as a discussion of SGR 0418+5729 below) and have led to the designation of these sources as magnetars. The presence of such strong magnetic fields and their role in powering the emission from AXPs and SGRs can also be inferred from a number of other arguments, as discussed in Section 2.1. The spectral and timing properties of all sources belonging to this category can be found in the online catalog maintained by the pulsar group at McGill University $\ddagger$ .

Even though SGRs were discovered through the recurrent bursts they produce in hard X-rays and soft gamma-rays (Mazets & Golenetskii 1981), and the AXPs were

$\ddagger$  <http://www.physics.mcgill.ca/pulsar/magnetar/main.html>

discovered through their persistent emission in the X-rays, by now, bursting behavior has been observed from nearly all of these sources (Gavriil, Kaspi, & Woods 2002). Within the magnetar model, the bursts are believed to be powered by the reconfiguration and dissipation of the magnetic field. The highly super-Eddington energy release of  $10^{44-45}$  erg in less than a second timescale points to a magnetospheric origin for these events (see Woods & Thompson 2004). On the other hand, the persistent emission originates deep in the crust and seems to be enhanced on year timescales following bursting activity (Kouveliotou et al. 2003) and glitches (Dib, Kaspi, & Gavriil 2008) and to be often correlated with changes in pulse profiles (Woods et al. 2004). In fact, the persistent X-ray emission in some sources shows such large excursions that they become detectable only during outbursts (Ibrahim et al. 2004). Long-term monitoring observations of these transient sources as well as during post-burst cooling of persistent sources has led to better understanding of crust cooling and energy injection mechanisms (e.g., Kouveliotou et al. 2003; Güver et al. 2007; Rea et al. 2009).

The surface emission from magnetars is primarily observable in the X-rays. The spectra are soft and broader than a blackbody, which has led to their empirical description by a blackbody plus power-law or two blackbody components. Hydrogen atmosphere models with high magnetic field strengths naturally generate such broad spectra (see Section 2.3). Reprocessing of the surface emission by mildly relativistic charges in the magnetosphere further broadens the spectrum and suppresses the equivalent widths of cyclotron features (Gavriil & Lyutikov 2006; Güver et al. 2007, 2008; Rea et al. 2008). Detailed comparisons of these models to observations have been successful and provide a spectroscopic measurement of the neutron star magnetic field strength (see Section 6).

Persistent emission has also been detected in the hard X-rays as well as in the optical and infrared wavebands (Hulleman, van Kerkwijk, & Kulkarni 2000; Kuiper, Hermsen, & Mendez 2004; Wang, Chakrabarty, & Kaplan 2008; see Mereghetti 2011b for a review of multiwavelength observations). Furthermore, there has also been a detection of transient pulsed radio emission from two AXPs (Camilo et al. 2004, 2006). All but the soft X-ray emission is thermodynamically inconsistent with originating from the neutron star surface (Özel 2004; Wachter et al. 2004) and has been attributed to non-thermal emission from the neutron star magnetosphere (Heyl & Hernquist 2005; Thompson & Beloborodov 2005; Baring & Harding 2007).

The X-ray pulse profiles of AXPs and SGRs have been studied in detail both during persistent emission and in connection to bursting activity (Woods et al. 2001; Gavriil & Kaspi 2002; Woods et al. 2004; Dib, Kaspi, & Gavriil 2007). The peak-to-peak amplitudes of pulsations range from 10%–80% and have been used to constrain the magnetar emission geometry (Özel, Psaltis, & Kaspi 2001). The pulse profiles have significant harmonic structure (see Figure 9), depend on photon energy, and evolve following bursting and glitching activity (Woods et al. 2004). These characteristics point to a non-dipolar magnetic field topology as well as magnetic field reconfiguration during bursts and glitches, as will be discussed in Section 6.

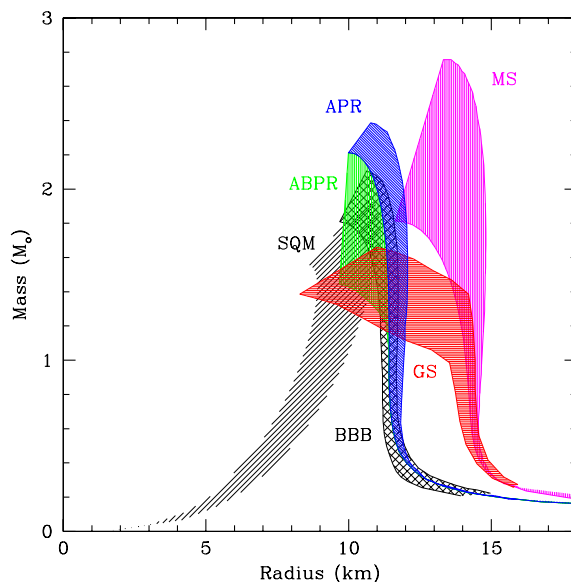


**Figure 10.** Mass-radius relations for a selection of neutron star equations of state. Each color-shaded region corresponds to a different calculation and represents a range of model parameters investigated in the corresponding study. APR is the nucleonic equations of state of Akmal et al. (1998) with the expansion in terms of 2- and 3- body interactions. MS is a field theoretical calculation with meson exchange interactions (Müller & Serot 1996). GS represents field theoretical calculations that incorporate a condensate of kaons (Glendenning & Schaffner-Bielich 1999). ABPR is a hybrid model based on the APR equation of state but incorporates a transition to quark matter at densities larger than  $\sim 2 - 3\rho_s$  (Alford et al. 2005). BBB represents a Brueckner-Hartree-Fock model. The equations of state that include strange quark matter are shown as the shaded region labeled SQM (Prakash et al. 1995).

#### 4. Neutron Star Radii and Compactness

One of the main goals of observing and modeling the surface emission from neutron stars has been to measure their radii and masses. These two macroscopic properties serve as direct probes of the microphysics of the neutron star interiors, which are characterized by densities significantly larger than the nuclear saturation density  $\rho_s \simeq 2.7 \times 10^{14} \text{ g cm}^{-3}$  and low temperatures. The physical conditions in the centers of neutron stars occupy a distinct region in the QCD phase diagram that cannot be probed by other cosmological observations or terrestrial experiments (e.g., Fukushima & Hatsuda 2011). Owing to the difficulties in determining the equation of state of neutron star matter from first principles, neutron star observations serve as an important constraint for determining the ultradense matter equation of state and for guiding calculations of the microphysics.

#### 4.1. Neutron Star Structure and Equation of State

A number of different approaches have been followed in the calculations of the equation of state of neutron star matter. A comprehensive overview of the methods and the details of the nuclear physics can be found in Glendenning 2000, Baldo & Burgio (2012) and Lattimer & Prakash (2001). Here, we provide a summary of the basic methods as well as a compilation of a few representative model equations of state.

One approach relies on determining the two-body potentials in the vicinity of  $\rho_s$  using nucleon-nucleon scattering data below 350 MeV and the properties of light nuclei, in addition to incorporating the contributions from the three-body potentials (Akmal, Pandharipande, & Ravenhall 1998; Morales, Pandharipande, Ravenhall 2002; Gandolfi, Carlson, & Reddy 2012). The expansion in terms of many body interactions, however, breaks down at densities larger than  $\rho_s$ . A second approach is based on field-theoretical calculations of constituents interacting via meson exchange (Müller & Serot 1996). A third approach involves microscopic ab initio calculations based on the Brueckner-Hartree-Fock model (Baldo, Bombaci, Burgio 1997) or its relativistic counterpart, the Dirac-Brueckner-Hartree-Fock model (Müther, Prakash, Ainsworth 1987).

In all of these calculations, the presence of additional components such as hyperons, mesons, or quark matter can be incorporated. For example, field-theoretical models have been developed that include hyperons (Glendenning & Moszkowski 1991) or kaon condensates (Glendenning & Schaffner-Bielich 1999). Non-relativistic potential models that allow quark degrees of freedom to appear at high densities in the cores of hybrid stars have also been investigated in great detail (e.g., Alford et al. 2005). Finally, there are models based on the assumption that the strange quark matter is the ultimate ground state of matter, which predict entire self-bound stars of up-down-strange quark matter, with stellar masses that increase with radius (Alcock, Farhi, & Olinto 1986; Prakash, Cook, & Lattimer 1995).

The equation of state of neutron star matter determines the macroscopic properties of the stars and, in particular, their masses and radii. In fact, there is a unique map between the microscopic pressure-density ( $P - \rho$ ) relation and the macroscopic mass-radius ( $M - R$ ) relation of stars (Lindblom 1992). In principle, the  $P - \rho$  relation can be obtained from astrophysical measurements of neutron star masses and radii by inverting this mapping. In practice, however, this requires a measurement of radii for neutron stars that span the entire range of masses between, e.g.,  $0.2 - 2M_\odot$ . Neutron stars with masses much smaller than the Chandrasekhar mass of the progenitor cores cannot be formed astrophysically (see the discussion in Özel et al. 2012), severely limiting the applicability of this direct inversion.

Even though the full functional form of the  $P - \rho$  relation cannot be mapped out from astrophysical observations, it has been shown that, for most model equations of state, neutron star masses and radii allow us to infer the pressure of ultradense matter at a few appropriately chosen densities above  $\rho_s$ . In particular, the radii at  $1.4 M_\odot$  lead primarily to the determination of the pressure at  $2\rho_s$  (Lattimer & Prakash 2001), the

slope of the mass-radius relation is most strongly affected by the pressure at  $4\rho_s$ , and the maximum mass of neutron stars is dictated by the pressure at  $\sim 8\rho_s$  (Read et al. 2009; Özel & Psaltis 2009). Therefore, measuring the masses and radii of even a small number of neutron stars can provide significant input to the microphysics calculations (Özel, Baym, & Güver 2010; Steiner, Lattimer, & Brown 2010).

Figure 10 shows the mass-radius relations for a number of equations of state representing the different approaches discussed above. For each equation of state, the shaded region represents the range of uncertainty in the mass-radius relations that are obtained for different input parameters within those calculations. The curves labeled APR correspond to a nucleonic equations of state with the expansion in terms of 2- and 3-body interactions and are characterized by radii that are nearly independent of the stellar mass (Akmal et al. 1998). The MS region is an example of a field theoretical calculation with meson exchange interactions; as in the case of APR relations, the radii are very weakly dependent on mass (Müller & Serot 1996). BBB is a representative Brueckner-Hartree-Fock model based on similar potentials as those incorporated in the APR equation of state and predict comparable dependence of mass on radius. The equations of state by Glendenning & Schaffner-Bielich (1999), which are the field theoretical calculations that incorporate a condensate of kaons, possess an inflection point at a characteristic density in the  $P - \rho$  relation. This manifests itself as a characteristic kink in the mass-radius relations of GS as shown in Figure 10 and reduces the predicted maximum mass neutron stars can support. Moreover, for the mass range of astrophysical interest, the radii become smaller with increasing stellar mass. Hybrid neutron stars with quark matter cores are represented by the region labeled ABPR, which is based on the APR equation of state but incorporates a transition to quark matter at densities larger than  $\sim 2 - 3\rho_s$  (Alford et al. 2005). Finally, the equations of state that include strange quark matter are shown as the shaded region SQM, characterized by a positive slope in the mass-radius relation (Prakash et al. 1995).

Measurements of neutron star radii and compactness have been achieved through observations and modeling of several different classes of sources. The number of independent observables, the uncertainties associated with each observable, and those in the theoretical models all play a role in determining the overall accuracy of the radii determinations. Below, I discuss the neutron star radius and compactness determinations by different techniques in various groups of sources. The first technique utilizes spectral data and includes radii measurements in accreting neutron stars during quiescence and during thermonuclear bursts. The second technique is based on modeling pulse profiles obtained from timing data and leads primarily to constraints on the neutron star compactness (mass-to-radius ratio) in accreting millisecond pulsars, millisecond radio pulsars, and stars that show flux oscillations during thermonuclear bursts.

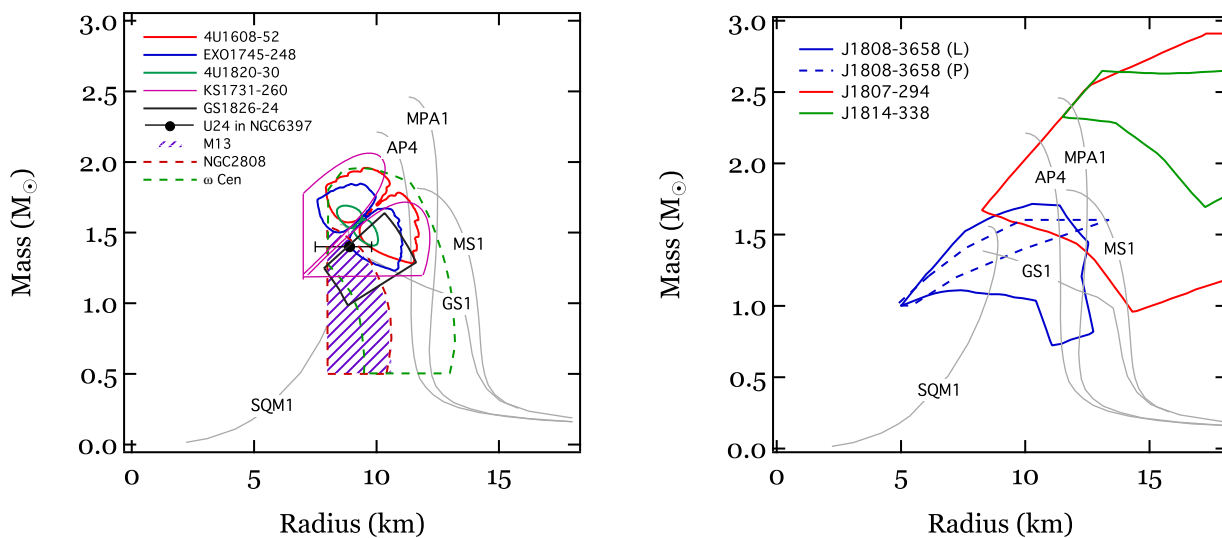


**Figure 11.** (*Left*) Radii measurements of neutron stars in quiescence and from thermonuclear bursts. All current measurements are consistent with radii in the range 8 – 12 km and disfavor neutron stars with  $\sim 15$  km radii. (*Right*) Constraints on neutron star masses and radii obtained from fitting pulse profiles of millisecond X-ray pulsars. The constraints for SAX J1808–3658 are from the independent analyses of Leahy et al. (2008, labeled L) and Poutanen & Gierlinski (2003, labeled P). In both panels, the labels follow the designation of Lattimer & Prakash (2001): AP4 represents the nucleonic equation of state of Akmal & Pandharipande (1997), MPA1 is a relativistic Dirac-Brueckner-Hartree-Fock model (Müther, Prakash, Ainsworth 1987), GS1 represents a field-theoretical calculation with a kaon condensate (Glendenning & Schaffner-Bielich 1999); MS1 is a typical meson exchange model (Müller & Serot 1996); and SQM1 represents a strange quark matter model (Prakash et al. 1995).

#### 4.2. Spectral Measurements

Numerous observations of accreting neutron stars during quiescence led, so far, to constraining determinations of apparent radii in a handful of sources. In particular, sources in globular clusters, to which distances can be measured through independent means, have primarily been selected for these studies. In addition, sources that show modest or negligible non-thermal components in their quiescent spectra and exhibit little variability between different quiescent episodes serve as the ideal targets for the radii and compactness measurements. In all the studies, atmosphere modeling yields apparent neutron star radii (see Equation 33), which are represented as correlated contours on the mass-radius plane. If a fixed (often arbitrary) neutron star mass, is assumed, the measurement of the apparent radius can be converted into a value for the neutron star radius. A compilation of the measurements performed to date is shown in Figure 11.

The quiescent emission from the source X7 in the globular cluster 47 Tucanae was modeled by Heinke et al. (2006) using non-magnetic hydrogen atmosphere models and the multiple observations obtained with the ACIS detector on board the Chandra X-ray



Observatory. They found a neutron star radius of  $R_{\text{NS}} = 14.5_{-1.4}^{+1.6}$  km, where the errors denote 90% confidence, when they kept the neutron star mass fixed at  $1.4 M_{\odot}$ . A caveat with this particular observation is that it suffered from severe pile-up ( $\sim 15\%$  level), which occurs when two or more photons arrive on the same pixel of the CCD within a read-out time and get recorded as a single photon, causing distortions in the observed spectrum. While pile-up corrections were applied in the analysis, the temperature inferred from the spectrum and the radii results are very sensitive to pile-up modeling. For this reason, this source is not included in Figure 11.

Webb & Barret (2007) applied a variety of hydrogen atmosphere models to three quiescent neutron stars in globular clusters. Their results on the neutron stars in M13, NGC 2808, and  $\omega$ Cen are shown in Figure 11. The absence of solutions with masses below  $0.5 M_{\odot}$  and radii less than 8 km reflects the range of model parameters that were not explored in the analysis. Webb & Barret found the most constrained radii in two of the sources:  $\leq 11$  km for M13 and  $\leq 10.5$  km for the neutron star in NGC 2808, where the uncertainty range reflects the formal errors at 90% confidence level in each fit; Webb & Barret also explore the small differences in the radii arising from fitting different atmosphere models to the spectra.

Figure 11 also shows the radius measurement for U24 in the globular cluster NGC 6397 (Guillot, Rutledge, & Brown 2011). Fitting hydrogen atmosphere models to the source spectra obtained during five different epochs, Guillot et al. (2011) found evidence for little flux variability between the epochs and  $\lesssim 5\%$  contribution from a power-law component. They reported an apparent radius of  $R_{\text{app}} = 11.9_{-0.8}^{+1.0}$  km, which corresponds to a neutron star radius of  $R_{\text{NS}} = 8.9_{-0.6}^{+0.9}$  km if its mass is assumed to be  $1.4 M_{\odot}$ .

A second category of sources in which radii measurements have been performed consists of neutron stars that show thermonuclear bursts (see Section 3.2). Because the bursts are observed in non-magnetic neutron stars as a result of unstable ignition of helium at the bottom of the accreted layer, the burning propagates rapidly ( $< 1$  s) across the surface of the neutron star and bright thermal emission is observed from the stellar surface for the duration of the burst. Several observables can be derived, in principle, from the spectra during bursts and can be used to determine the neutron star radius (see van Paradijs 1979; Damen et al. 1990; Özel 2006). They are (i) the redshifts of atomic lines in burst spectra (ii) the apparent radii of thermal emission during burst cooling, which can be fit with atmosphere models for accreting, bursting neutron stars, and (iii) the Eddington limit in bright, so-called photospheric radius expansion bursts.

The only measurement of gravitationally redshifted atomic lines with a high resolution instrument was reported by Cottam, Paerels, & Mendez (2002), who analyzed combined spectra from 28 bursts from the neutron star in EXO 0748–676. Özel (2006) made use of the redshift measurement in conjunction with the apparent radii determined during the cooling phases of the thermonuclear bursts from this source and obtained a neutron star radius of  $R = 13.8 \pm 1.8$  km. However, a subsequent discovery of the spin period of the neutron star called into question the consistency between the width of the observed lines and the width expected from stellar rotation (Galloway et al. 2010; Lin

et al. 2010), rendering the redshift measurement in EXO 0748–676 untenable.

The uniformity and the reproducibility of emission from the stellar surface are key ingredients for performing radius measurements from thermonuclear bursts. The large number of bursts observed with RXTE, BeppoSAX, Chandra, and XMM-Newton has allowed these hypotheses to be observationally tested. Indeed, an analysis of the large database of burst observations found that the spectra are thermal and that, for numerous sources, the apparent radius is consistent to within 3 – 8% during the cooling tail in each burst and between bursts observed from each source (Güver et al. 2012b; a small number of outlier bursts with larger variations have been observed in some sources and are discussed in detail in Güver et al. 2012b; Bhattacharyya, Miller, & Galloway 2010; Zhang, Mendez, & Altamirano 2011). In addition, the Eddington flux was also shown to be reproducible to 10% (Güver et al. 2012a; see also Kuulkers et al. 2003).

The apparent radii of neutron stars are measured during the cooling tails of thermonuclear bursts by making use of bursting neutron star atmosphere models for a range of compositions and depend on the stellar mass and radius through Equation (33). The Eddington fluxes, measured in bright bursts that show photospheric radius expansion, have a different dependence on mass and radius, as shown in Equation (37). The combination of these measurements, together with an estimate of the distance to each source, has led to the determination of the neutron star radii in a number of bursters to date, with weakly correlated errors (Özel, Güver, & Psaltis 2009; Güver et al. 2010a; Güver et al. 2010b; Özel, Gould, & Güver 2012). The results for 4U 1608–52, KS 1731-260, EXO 1745–248, and 4U 1820-30 are shown in Figure 11. The radii are tightly clustered, with a 90% confidence range spanning  $R = 8 - 11$  km.

A different approach to measuring radii using burst spectra was employed by Majczyna & Madej (2005) and Zamfir, Cumming, & Galloway (2011). Majczyna & Madej (2005) modeled the distortions in the burst spectra of 4U 1728–34 obtained with RXTE as a function of surface gravity and redshift of the neutron star and converted the constraints on these two parameters to constraints on the neutron star radius, which yielded, at 90% confidence level,  $R \lesssim 11$  km for this source. Because the distortions to the spectrum due to changing surface gravity are marginal and the RXTE energy resolution is not adequate to detect such small deviations, this measurement is highly uncertain. Zamfir et al. (2011), on the other hand, studied the evolution of the spectra as a function of the declining flux during the cooling tail of the bursts from GS 1826–24. The radius constraints they obtained, which span  $R \simeq 8 - 12$  km, are shown in Figure 11. Suleimanov et al. (2011) attempted a similar study on one burst from 4U 1724–307; however, the spectra from this burst are inconsistent with thermal spectra, showing evidence for atomic edges and a reflection component (in’t Zand & Weinberg 2010), making the radius derived in this study also highly uncertain (see the discussion in the appendix of Güver et al. 2012b).

Spectral modeling of surface emission from a number of isolated sources such as RX J1856.5–3754 (e.g., Drake et al. 2002; Braje & Romani 2002; Ho 2007) and Cas A (Ho & Heinke 2009) has also been performed. Several of these studies incorporate

different elemental abundances (e.g., C atmospheres, see Ho & Heinke 2009) and physical conditions (e.g., magnetized condensed surfaces, see Turolla, Zane, & Drake 2004). The inconclusive phenomenology of their X-ray emission, uncertainties in the importance of their magnetic fields, as well as the low count rates have led only to weak constraints on the radii of these neutron stars. However, these sources still provide important information about the interiors of the neutron stars through their inferred cooling histories, as will be discussed in Section 5.1.

It is remarkable that radii measurements obtained on nine different sources, using at least three distinct spectroscopic methods, during bursts and in quiescence, result in a narrow range of values, with a clear upper limit of 12 km.

### 4.3. Pulse Profile Fitting

In this category, there are constraints on neutron star radii and/or compactness ratio that result from modeling lightcurves of millisecond X-ray or millisecond radio pulsars. In the case of accreting millisecond X-ray pulsars, the quasi-thermal emission originates from the base of the accretion column, which is then Comptonized in the column (Poutanen & Gierlinski 2003; see section 3.3). Similarly, in addition to non-thermal emission from their magnetospheres, rotation-powered millisecond pulsars show a predominant thermal component in the soft X-rays (Grindlay et al. 2002; Zavlin 2006; 2007; Bogdanov et al. 2006a). By modeling the shapes and amplitudes of the pulses from these surface hotspots, and taking into account the gravitational bending of light and Doppler boosting due to the stellar rotation, both of which depend on the stellar compactness, constraints on this parameter can be obtained. The lightcurves also depend on the location of the hotspots and the line of sight of the observer with respect to the rotation axis, as well as on the size of the hotspot. Therefore, lightcurve fits constrain a combination of all of these parameters and result in measurements of these parameters with correlated uncertainties.

This method has been applied to three accreting millisecond X-ray pulsars: SAX J1808.4–3658 (Poutanen & Gierlinski 2003; Leahy, Morsink & Cadeau 2008; Morsink & Leahy 2011), XTE J1814–338 (Leahy et al. 2009), and XTE J1807–294 (Leahy, Morsink, & Chou 2011). The constraints on the mass and radius of the neutron stars inferred in these studies are shown together in Figure 11. The contours depict 99% confidence levels. The large uncertainties in the mass-radius measurements shown in this figure reflect the influence of the various geometric factors discussed above, which are difficult to constrain.

X-ray data from a number of millisecond radio pulsars, obtained with ROSAT, Chandra, and XMM-Newton, have been analyzed using hydrogen atmosphere models for the thermal emission from a polar cap (see, e.g., Zavlin & Pavlov 1998). In these models, pulse profiles are calculated based on the beaming of radiation predicted by the theoretical models. For PSR J0437–4715, Bogdanov, Rybicki, & Grindlay (2007) obtain  $R=6.8-13.8$  km (90% confidence) for a neutron star mass of  $1.4 M_{\odot}$  (see also Pavlov &

Zavlin 1997). However, a subsequent measurement of a  $1.76 M_{\odot}$  mass (Verbiest et al. 2008) set a lower limit on its radius to  $R > 8.3$  km (99.9% confidence). For pulsars PSR J2124–3358 and PSR J0030+0451, similar analyses lead to a lower limit on their radii of 7.8 km (68% confidence) and 10.7 km (95% confidence), respectively, assuming a stellar mass of  $1.4 M_{\odot}$ .

Strong X-ray pulsations originating from the surfaces of neutron stars have also been detected during thermonuclear X-ray bursts (Strohmayer 1996). Modeling the pulse profiles of these burst oscillations can also lead to constraints on the neutron star compactness (see Weinberg, Miller & Lamb 2001 and references therein). In particular, the amplitude of the oscillations, the deviations from a sinusoidal waveform, and their dependence on photon energy can be probes of the neutron star radius and mass (see, e.g., Weinberg et al. 2001; Munro et al. 2002, 2003). This technique was applied to oscillations observed from 4U 1636–536 (Nath, Strohmayer, & Swank 2002) and from XTE J1814–338 (Bhattacharyya et al. 2005). For the case of 4U 1636–536, assigning the oscillation frequency to the neutron star spin frequency, as has been later demonstrated, led to no significant constraints on the compactness of the neutron star. On the other hand, Bhattacharyya et al. (2005) report a limit of  $R > 4.2GM/c^2$  (90% confidence level) for the neutron star in XTE J1814–338, based on fitting its pulse profile.

As I will discuss in Section 8, pulse profile modeling is a potentially powerful probe of the neutron star compactness and radius, which will be exploited by future X-ray timing satellites with high signal-to-noise capabilities.

## 5. The Composition of the Neutron Star Interior and Its Crust

Observations of thermal emission from young, cooling neutron stars as well as from transiently accreting neutron stars in quiescence have been used to track neutron star cooling and probe their internal composition and equation of state.

As discussed in Section 2.1, neutron star cooling depends sensitively on the properties and interactions of the dense neutron star interior as well as on the composition of the stellar crust (see Figure 1). Cooling models are divided into three broad categories: the standard cooling models, which incorporate modified Urca and nucleon-nucleon bremsstrahlung processes for neutrino emission and predict the slowest cooling rates; the minimal cooling models, which take into account additional neutrino emission from the breaking and formation of Cooper pairs in the superfluid core and lead to moderate cooling rates in a limited temperature range; and enhanced cooling models, which include direct Urca processes and lead to the lowest surface temperatures and the shortest thermal emission timescales. The cooling rate also depends on the composition of the envelope and, in particular, of a thin layer within the envelope in which the ions are in liquid phase (see Figure 1). As a general trend, neutron stars with higher central densities (which occurs in the cores of higher mass stars) and with light element envelopes cool faster. Furthermore, in neutrino cooling calculations with superfluid

baryons, models with higher critical temperatures allow larger neutrino emissivity and cool more rapidly. Therefore, observations of the thermal emission of cooling neutron stars with different ages can potentially provide information about the neutron star interior at supernuclear densities as well as the composition of the neutron star crust. Finally, the critical temperature at which the transition to superfluidity occurs can be probed by comparison of cooling curves with data (Yakovlev & Pethick 2004).

Making a meaningful comparison between observations and cooling curves requires the measurement of three quantities for each neutron star: the effective temperature, the distance, and the time since the cooling commences. For isolated neutron stars, the latter is the age of the neutron star, while in X-ray transients, it is the time since the last outburst.

The temperature of the surface emission is obtained from fitting atmospheric models to the observed spectra. The angular sizes inferred from these fits are converted into an emitting area using additional information regarding the distance to the source. For young isolated sources, the non-uniformity of surface emission as well as the significant contribution from non-thermal magnetospheric emission, and in several cases, the emission from a supernova remnant, complicate the temperature determination. In addition, for some sources, realistic (light element) atmosphere models do not yield emitting areas that can be obtained with reasonable neutron star radii (Chang & Bildsten 2003; Page et al. 2004). This could be due to systematic uncertainties in the source distances, low signal-to-noise in sources with faint thermal components, which introduces uncertainties in the temperature measurement, or uncertain subtraction of the non-thermal emission components. Finally, owing to the higher magnetic field strengths in pulsars, which affects cooling rates as well as heat transport in the crust, it may be challenging to map the surface temperature distribution from the spectra. In accreting sources, similar concerns with non-thermal components arise due to accretion or emission from the binary companion. In that case, selecting sources with the smallest level of non-thermal components in the spectra and the smallest amount of variation in the quiescent flux levels between different outburst episodes help reduce the uncertainties in the measured effective temperatures.

Distance measurements come from a variety of techniques. For a handful of nearby sources, parallax measurements yield reliable distances (see the References in Table 5). Pulsar dispersion measures are also a common way to obtain distance estimates to isolated sources. For sources associated with supernova remnants, the distance estimates to supernova remnants are taken as the source distances. Finally, in the absence of direct distance determinations, interstellar absorption measurements to other nearby stars are utilized. For neutron star X-ray transients that are located within globular clusters, optical observations of the stars in the cluster provide some of the better constrained source distances. Distance measurements are used in conjunction with the thermal fluxes to compare them with cooling curves that track the evolution of luminosity with time.

For isolated sources, the ages of neutron stars are inferred via their associations

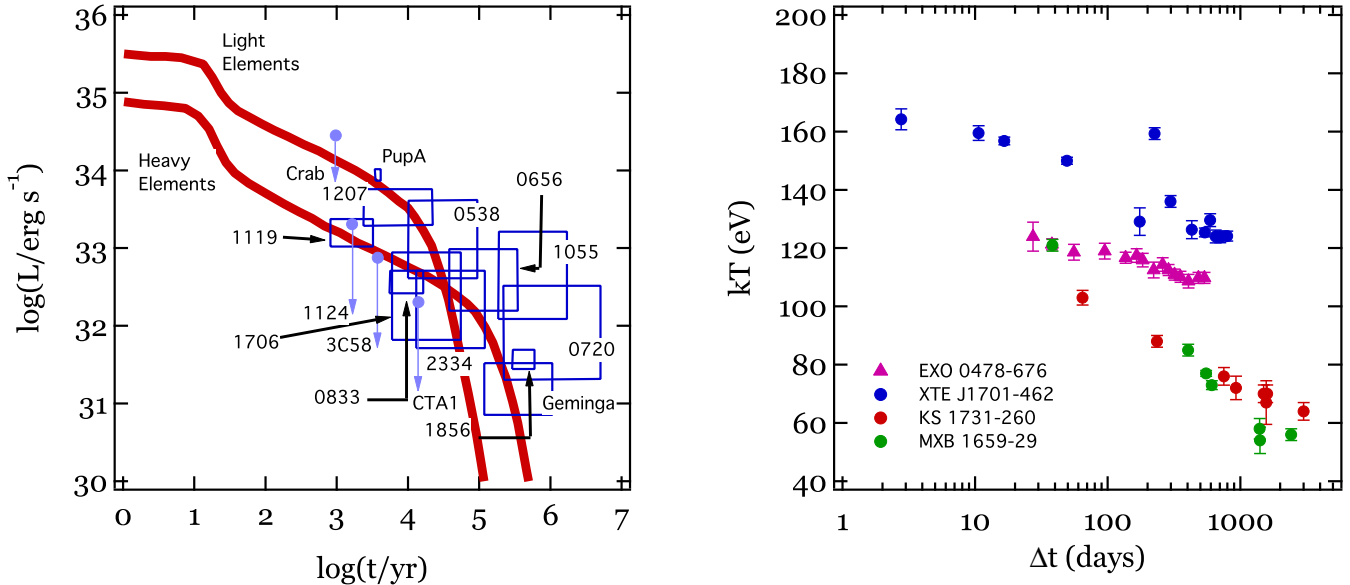


**Figure 12.** (Left) Cooling curves for different compositions of the neutron star envelope and data on young cooling neutron stars, adapted from Page et al. (2009). For visual clarity, source names have been abbreviated in the figure. (Right) The evolution of the inferred neutron star temperature in four neutron-star X-ray transients during quiescence, adapted from Degenaar et al. (2011b).

with supernova remnants, their kinematic properties, or their spindown rates (Table 5). It is well known that the measurements via these different methods seldom agree (e.g., Gaensler & Frail 2000). For pulsars, ages are estimated from the observed spindown rate  $t_{\text{sd}} \equiv P/2\dot{P}$ , which assumes that pulsars are born with spin periods much smaller than their currently measured period  $P$  and that the spindown torque is due only to a dipole magnetic field. The kinematic ages in a handful of sources are obtained from the combination of pulsar transverse velocities and their distances to a likely site of origin, such as the center of an associated supernova remnant or a nearby massive star cluster. There are unquantified uncertainties associated with each method, which remain the primary challenge in comparing young cooling neutron stars to theoretical cooling curves. In X-ray transients, cooling is tracked from the moment when the outburst ceases and the source enters a quiescent period, which is determined primarily by X-ray monitoring observations and introduces less uncertainties in cooling times.

### 5.1. Comparison of Cooling Models to Thermal Evolution of Isolated Neutron Stars

Isolated neutron star sources for which measurements of a surface temperature, a characteristic age, and distance exist are shown in Figure 12 and discussed in Table 5. In the left panel, the isolated sources are compared with two minimal cooling curves obtained for different envelope compositions. In these particular models, the neutron star is assumed to have a mass of  $1.4 M_{\odot}$  with the APR equation of state, and the neutron  ${}^3P_2$  gap in superfluidity is chosen such that the neutrino cooling rate due

to Cooper pair formation and breaking is high (case “a” in Page et al. 2004). The sources include four known pulsars with only upper limits on their thermal emission. Even though more stringent upper limits exist for compact central sources in supernova remnants (see Page et al. 2009), their neutron star nature is not established because no pulsations have been detected. For this reason, they have been excluded from this figure.

It is evident from the comparison of the data with the cooling curves in this figure as well as in Figure 1 that fast cooling, as would be predicted by direct Urca processes, is inconsistent with the high temperatures observed in neutron stars in the  $10^4 - 10^6$  yr age range. In addition, the high surface temperatures observed in the young neutron stars PSR 1E1207–52 and the PSR J0822–4247 (in remnant Puppis A) require light element envelopes with no fast neutrino emission processes in the cores. However, the upper limits in the thermal emission from three compact objects known to be neutron stars (PSR J1124–5916, the pulsar in 3C58, and the pulsar in CTA1) as well as the emission observed from the Vela pulsar are barely consistent with the predictions of minimal cooling with heavy element envelopes.

With the data currently available, it becomes evident that there exists no single universal cooling curve followed by all neutron stars. This is not surprising given that different neutron stars may have a range of masses, different envelope compositions, or a range of magnetic field strengths. It is not clear from the current data which of all these parameters produces the dominant difference in cooling histories. A range of neutron star masses can account for some of the observed differences (e.g., Yakovlev & Pethick 2004) and has, in fact, been suggested as a way of distinguishing between neutron stars of different masses (Kaminker et al. 2001). Heterogeneity in the composition of neutron star envelopes also allows cooling models to account for the bright young pulsars as well as for pulsars with significant thermal emission at ages greater than a million years (Page et al. 2009).

Because the cooling timescales are very long, the comparison of the cooling curves to data discussed above has been made possible by combining the thermal properties of neutron stars at different ages instead of tracking the temperature evolution of individual neutron stars with time. The only exception in isolated cooling sources is the observations by Chandra of the very young source in supernova remnant Cas A, which showed a temperature decrease of  $\sim 80000$  K, from  $2.12 \times 10^6$  K to  $2.04 \times 10^6$  K, over a time of  $\sim 10$  years (Heinke & Ho 2010). The main evidence that this source might be a neutron star is the carbon atmosphere modeling of its surface spectrum (Ho & Heinke 2009). Within this interpretation, the temperature at 330 years of age is too high to be driven by direct Urca processes but the time evolution of the temperature is too steep for the standard cooling scenario. This steep temperature gradient has been attributed to a transition to superfluidity in the core of the neutron star within the minimum cooling paradigm (Page et al. 2011; Shternin et al. 2011).

### 5.2. Results for Neutron Star Transients in Quiescence

In contrast to isolated cooling neutron stars, in the case of accreting neutron stars, theoretical cooling curves have been compared to the temperature evolution of individual sources as they enter quiescence. This is because both the thermal relaxation timescale of the crust as well as the recurrence timescale of quiescent episodes are in general short enough to allow detectable changes in the source temperature over the timescale of the observations.

Clear evidence for the thermal evolution of the crust is present in the observations of four neutron stars out of approximately a dozen sources that have been monitored in quiescence (see Table 2). These sources are KS 1731–260 (Cackett et al. 2010a), MXB 1659–29 (Cackett et al. 2008), XTE J1701–462 (Fridriksson et al. 2011), and EXO 0748–676 (Degenaar et al. 2011b; Diaz-Trigo et al. 2011) and are distinguished from the other neutron stars in quiescence for two reasons. First, they have prolonged periods of outbursts, which deposit sufficient energy to drive their crusts out of thermal equilibrium with their cores. Second, their quiescent emission is characterized by relatively low variability and, in general, a weak contribution from non-thermal processes, allowing the surface temperature to be measured more accurately. The evolution of the inferred surface temperature with time is shown in Figure 12 for these four sources. Detailed modeling of the rapid decline in the surface temperature in the first two sources in this list revealed that there is efficient conduction of heat in the crust, which, in turn, indicates low levels of impurities in the ion lattice (Shternin et al. 2007; Brown & Cumming 2009). The same is true for the rapid cooling observed in XTE J1701–462 (Fridriksson et al. 2010; see, however, Page & Reddy 2012 for an alternate interpretation). In contrast, EXO 0748–676 shows a very mild decline in its temperature, which may be related to its different outburst characteristics compared to those of the other three sources or the presence of a hotter core (Degenaar et al. 2011b). Monitoring of the thermal evolution of the more recently discovered sources during their quiescence, such as IGR J17480–2446 (Degenaar et al. 2011a) may help increase this sample.

While tracking the temperature decline during quiescence reveals the thermal relaxation of the crust, studies of the long-term time averaged outburst luminosities and the asymptotic quiescent luminosities may probe the thermal properties of the stellar core (see, e.g., Yakovlev et al. 2003). The core temperature is sensitive only to the long-term time-averaged mass accretion rate because the thermal relaxation timescale of the core is  $\sim 10^4$  years. A comparison of the asymptotic quiescent luminosity, which accounts for the energy stored in the stellar interior and is subsequently reradiated in photons, to the average outburst luminosity, which represents the total accretion energy available, yields estimates of the storage efficiency  $f$  (see Equation 2). Even though there are large variations in the observed storage efficiencies, they are in general low (see, e.g., Page & Reddy 2006) and indicate that a large fraction of the accretion energy is radiated efficiently from the stellar interior via neutrinos.



## 6. Neutron Star Magnetic Field Geometry and Evolution

Studies of the thermal emission and the atmospheres of neutron stars that aim to constrain the strength, geometry, and the evolution of their magnetic fields have so far been performed for isolated radio and X-ray pulsars, as well as AXPs and SGRs. Other lines of evidence that do not rely on the properties of surface emission, such as the occurrence of thermonuclear bursts or the lack of pulsations, have been used to infer the magnetic field strengths of accreting neutron stars but will not be reviewed here.

A general result that is common to the studies of the different types of moderate to high magnetic field strength sources is that modeling the pulse profiles in nearly all cases points to a complex, non-dipolar magnetic field geometry.

The pulsed thermal emission that has been observed from a wide variety of neutron stars, such as isolated and millisecond radio pulsars and isolated X-ray pulsars, has been modeled by one or two circular hotspots that correspond to the magnetic poles on a neutron star, the rest of which is taken to be too cold to contribute to the surface emission. The pulse profiles are then computed for varying sizes and temperatures of the magnetic poles, the observer's line of sight, taking into account the general relativistic bending of light and compared to the thermal emission from pulsars (e.g., Page 1995; Zane et al. 2006). Further complexities in the models include offset dipolar geometry, where the magnetic poles are not taken to be antipodal, temperature gradients in the polar caps, which may be due to a variation in the field strength, different temperatures on the two magnetic poles, or emission geometries that are motivated by different multipole fields. The application of these models to pulsar pulse profiles yielded evidence for complex field topology and emission geometries for a number of sources, such as non-uniform temperature on polar caps in PSR J0437–4715 (Zavlin & Pavlov 1998), significantly different temperatures on two antipodal caps in PSR J0822–4247 (Gotthelf, Perna, & Halpern 2010), offset dipole field in the millisecond radio pulsar PSR J0030+0451 (Bogdanov & Grindlay 2009), as well as non-dipolar field topology in the isolated neutron star RX J0720.4–3125 (Pérez-Azorín et al. 2006), in the “three musketeers”, i.e., the three radio pulsars that showed clear evidence for surface emission in ROSAT observations (De Luca et al. 2005), and in the Geminga pulsar (Page, Shibano, & Zavlin 1995).

Modeling pulse profiles of magnetars, which have been monitored both during quiescence and in connection to bursting activity, also point to a complex and evolving magnetic field topology. Pulse profiles of AXPs and SGRs, which can be stable over a timescale of years, show multiple peaks, a high pulsed fraction, as well as significant substructure (e.g., Gavriil & Kaspi 2002). However, both long-term evolution (Dib et al. 2007) and sudden changes in the pulse morphology have been observed. The latter point to magnetic field reconfiguration that accompany or are triggered by bursts and outbursts in these sources: for example, a sudden change in the pulse profile in SGR 1900+14 accompanied a flux increase of nearly three orders of magnitude and persisted as the flux decayed (Woods et al. 2001). In AXP 1E 2259.1+586, more than 80

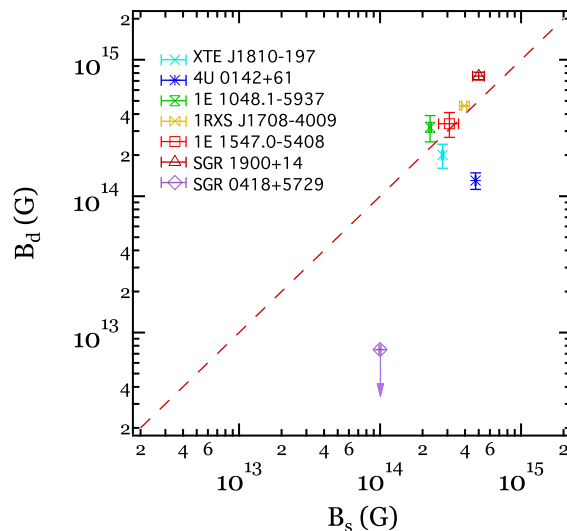


**Figure 13.** The dipole magnetic field strengths of AXPs and SGRs inferred from their rate of spindown using Equation 7 plotted against their surface field strengths measured by fitting their thermal continuum spectra with highly magnetic neutron star atmosphere models.

individual bursts were detected at the onset of an outburst that included major changes in the pulse profile and persistent flux (Woods et al. 2004). Pulse profile modeling with one or two magnetic poles help constrain the magnetic field geometry as well as the size and the temperature of the polar caps in magnetars (Özel 2002).

Magnetars are unique in that, owing to their very strong magnetic fields, physical processes that take place in this regime imprint particular characteristics on their thermal continuum spectra, as discussed in Section 2.3. Therefore, in the case of AXPs and SGRs, the spectra provide a handle on the magnetic field strength on the neutron star surface. The magnetic field strengths of numerous sources have been measured by modeling their spectra with strongly magnetic neutron star atmosphere models (Güver et al. 2007, 2008; Özel et al. 2008; Göğüş et al. 2011; Ng et al. 2011; Güver et al. 2011). The dipole magnetic field strength  $B_d$  inferred from their measured rate of spindown using Equation 7 is plotted against the spectroscopic magnetic field strengths  $B_s$  obtained for these sources in Figure 13. In the majority of the sources, the two magnetic field strengths are comparable to each other, lying close to the  $B_s = B_d$  line shown in the figure. Furthermore, the spectroscopic field strengths determined from spectra obtained during different epochs from XTE J1810–197, when the source progressed through significantly different flux levels, agree remarkably well (Güver et al. 2007). Interestingly, detailed modeling of the pulse profiles of this AXP, which has the pulse profile with the least structure (see Figure 9), reveals that its magnetic field topology is consistent with a dipolar geometry (Perna & Gotthelf 2008).

The notable exception to the similarity between the spindown and spectroscopic field strengths is SGR 0418+5729. Despite a spectroscopically inferred surface field of

$10^{14}$  G and other properties that closely resemble all other SGRs, its period derivative is so small that the current upper limit on  $\dot{P}$  yields an upper limit on its dipole magnetic field strength of  $7.5 \times 10^{12}$  G (Rea et al. 2010). This has been interpreted as evidence for a highly non-dipolar field that is dominant on the neutron star surface and that shapes the surface emission and the characteristics of the energetic bursts (Rea et al. 2010; Güver et al. 2011).

## 7. Complementary Approaches to Neutron Star Physics

This review focused on the physics of the surface emission from neutron stars and the implications of the current observations for the neutron star interior and crust. There are, however, numerous other astrophysical probes of neutron star properties that have been pursued during the last decade and provide complementary information on neutron star physics. I will provide a here a brief discussion of these additional tools.

Neutron star masses have been measured with the highest precision using pulsar timing techniques (see the review by Kramer 2008 for details). The most constraining aspect of the mass measurements from the point of view of neutron star physics is finding the heaviest pulsar, which sets a lower bound on the maximum mass of neutron stars. The maximum mass is a key constraint on the dense matter equation of state. It is a consequence of general relativity and is determined primarily by the stiffness of dense matter at densities larger than  $\sim 4\rho_{\text{sat}}$ . The current record holder is PSR J1614–2230 with a mass of  $M = 1.97 \pm 0.04 M_{\odot}$  (Demorest et al. 2010). Such a large mass already argues against significant softening of the equation of state by the emergence of new degrees of freedom at high densities (Özel et al. 2010). Mass measurements of a large sample of neutron stars also reveal their intrinsic mass distribution and probe the physics of the supernova explosions and neutron star formation (Thorsett & Chakrabarty 1999; Kiziltan et al. 2011; Zhang et al. 2011; Özel et al. 2012).

Long-term monitoring of radio pulsars has also shown that they undergo secular spindown interrupted by sudden glitches (see Espinoza et al. 2011 and references therein). These glitches have been interpreted as sudden transfer of angular momentum from superfluid neutrons in the interior of the star to the outer crust (Anderson & Itoh 1975). The observed magnitudes of the glitches have been used to place constraints on the relative moment of inertia between the crust and the core. In the case of the Vela pulsar, which has shown prolific glitches, measurements indicate that  $\geq 1.4\%$  of the neutron star’s moment of inertia drives these glitches. This translates into a lower bound on the radius of 8.9 km for a neutron star with mass  $> 1.35 M_{\odot}$  (Link, Epstein, & Lattimer 1999).

An independent constraint on the masses and radii of accreting neutron stars arises from the observations of fast quasi-periodic oscillations (QPOs) in their X-ray brightness (van der Klis 2000). The frequencies of these oscillations are variable but can be as high as  $\simeq 1330$  Hz, strongly suggesting that they occur in the accretion flow very close to the neutron star surfaces. Requiring that an observed QPO frequency is lower than the

Keplerian frequency at the neutron star surface, which is the largest possible dynamical frequency in the exterior spacetime of the neutron star, places an upper bound on the stellar radius (Miller, Lamb, & Psaltis 1998). For most equations of state, however, the neutron star radii are smaller than the radius of the innermost stable circular orbit in their spacetimes. For this reason, the maximum possible stable dynamical frequency in the exterior of a neutron star is the Keplerian frequency at the location of the innermost stable circular orbit, which depends primarily on the neutron star mass. Therefore, requiring that an observed QPO frequency is lower than this maximum stable frequency also places an upper bound on the neutron star mass (Kluźniak, Michelson, & Wagoner 1990; Miller et al. 1998). The maximum observed QPO frequency currently stands at  $\simeq 1330$  Hz and provides only weak upper limits on the neutron star radius of  $\leq 15$  km (van Straaten et al. 2000; see also Boutelier et al. 2009).

Precise measurements of neutron star masses are, in principle, possible via observations of QPO frequencies but only within a particular model for their interpretation. For example, the rapid decline of the amplitude and coherences of QPOs observed at high frequencies have been interpreted as signatures of the innermost stable circular orbit. Identifying the QPO frequency with the Keplerian frequency at that radius leads to a direct measurement of the neutron star mass (e.g., Barret, Olive, & Miller 2006). On the other hand, modeling the observed correlations (Psaltis, Belloni, & van der Klis 1999) between the frequencies of different QPOs in the same source within models that assign their frequencies to epicyclic motions in the neutron star spacetimes lead to different inferences for the neutron star masses (e.g., Stella, Vietri, & Morsink 1999). All such mass measurements are, by construction, model dependent and can only be considered as preliminary at this time, pending validation of the theoretical model within which they were obtained.

A different bound on the inner radius of the accretion disk, and therefore, on the radius and mass of the neutron star, comes from observations of relativistically broadened iron fluorescence lines in the X-ray spectra of accreting neutron stars (Cackett et al. 2010c). Interpreting these observations requires detailed models of the fluorescence yield as a function of radius in the accretion flow as well as assumptions about the ionization state and the origin of the incident radiation on the disk. Current analyses impose a lower limit on the inner edge of the accretion disk of  $6 GM/c^2$  and find that in at least two neutron stars (4U 1636–53 and HETE J1900.1–2455), the neutron star radius has to be smaller than this limit (Cackett et al. 2010c).

## 8. Future Outlook

During the last decade, tremendous progress has taken place in the understanding of neutron stars through observations and modeling of their surface emission. Not only the number but also the classes of neutron stars that show thermal emission have dramatically increased with the discovery of sources such as nearby isolated neutron stars, magnetars, and millisecond accreting X-ray pulsars. These discoveries were made

possible primarily through X-ray satellites such as the Rossi X-ray Timing Explorer, the Chandra X-ray Observatory, and XMM-Newton that improved the timing, spectral, and imaging capabilities of earlier instruments by orders of magnitude.

An equal amount of progress has been achieved in theoretical calculations of neutron star atmospheres and their emission characteristics. The new studies significantly widened the parameter space in neutron star properties that have been explored and incorporated different regimes of magnetic field strengths from unmagnetized stars to magnetars, different compositions and states of matter from cold lattices to fully ionized plasmas, and a variety of mechanisms that power the surface emission from particle bombardment to magnetic field decay. Moreover, the connections between the macroscopic properties of neutron stars and the physics of their interiors have been strengthened to the point that neutron star observations can provide tight constraints on basic parameters that describe the physics of ultradense matter such as the pressure at several times the nuclear saturation density and the critical temperature for the transition to superfluidity in the neutron star core.

Current observations provide tantalizing hints of spectral lines from the atmospheres of different types of neutron stars. Identification of these lines either with atomic transitions or cyclotron features has not been conclusive. Future observations with upcoming detectors that have larger collecting areas and high spectral energy resolution, such as Astro-H (Takahashi et al. 2010) and proposed missions including ATHENA have the potential of detecting a multitude of lines that can be identified and used to measure neutron star properties. More specialized detectors that will measure the polarization properties of neutron star surface emission can provide additional handles on the magnetic field structure and geometry of neutron stars.

A second promising avenue towards obtaining independent constraints on the masses and radii of neutron stars is via modeling of the pulse profiles generated from non-uniform emission from the surface of a rotating neutron star. Current investigations have developed a theoretical framework that takes into account the effects of general relativistic light bending in the rotating spacetimes of neutron stars that have been applied primarily to observations of accreting millisecond pulsars and to magnetic neutron stars. The optimal setting for such studies is during the first fraction of a second of a thermonuclear burst on a weakly magnetic neutron star. In this case, the shape and the temperature profile of the small burning area immediately after ignition has the least effect on the pulse profile, which is determined primarily by general relativistic effects. Observations of neutron stars with the high timing resolution and the large collecting area afforded by the planned mission LOFT (Feroci et al. 2011) will make such measurements possible in the near future.

The largest uncertainty in several of the measurements discussed in this review, such as the cooling curves of neutron stars and the radius determinations from thermally emitting stars, arises from the poorly constrained distances to these sources. This is especially problematic for sources in the Galactic disk, for which very few handles on their distance are available. The situation will dramatically change with the launch of

GAIA (Turon, O’Flaherty, & Perryman 2005) that will chart the three-dimensional map of the Galaxy and measure the distance to a large number of sources, especially to those with binary companions.

The improvements in the observations and modeling of diverse phenomena from the surfaces of neutron stars will tighten the uncertainties in the neutron star properties inferred from each measurement. Moreover, the detection of multiple phenomena from each neutron star, e.g., thermonuclear bursts, quiescent emission, and burst oscillations, will eventually lead to independent measurements of neutron star masses and radii. This can then be used to test the consistency of the various measurements and explore the systematic uncertainties in each technique. In addition, as measurements become overconstrained, they offer the possibility of testing the predictions of general relativity for the strong gravitational fields in the vicinity of neutron star surfaces (Cooney, DeDeo, & Psaltis 2010; Deliduman, Ekşi, & Keleş 2011; see also Psaltis 2008 for a review).

Several complementary probes of neutron star physics that do not rely on the emission from their surfaces will become available in the near future. Ongoing searches for the fastest spinning neutron stars may detect pulsars spinning at sub-millisecond periods and, hence, place strong upper limits on the radii of neutron stars (Cook, Shapiro, & Teukolsky 1994). Long-term observations of the double pulsar will allow for a measurement of the moment of inertia of one of the pulsars and, therefore, constrain the density profile of its interior (Kramer & Wex 2009). Neutrino detectors may observe the burst of neutrinos that are emitted during the formation of a proto-neutron star in a supernova explosion and provide information on not only the mechanism of the explosion itself but also on the equation of state of ultradense matter (see Kotake, Sato, & Takahashi 2006). Finally, detection of gravitational waves during the coalescence of two neutron stars or the inspiraling of a neutron star into a black hole will open a new window into the neutron star structure and equation of state (e.g., Read et al. 2009; Pannarale et al. 2011).

## Acknowledgments

I am grateful to Dimitrios Psaltis for numerous useful discussions and Gordon Baym for helpful guidance. I thank Joel Fridriksson, Dany Page, and Tolga Güver for carefully reading and providing detailed comments on the manuscript. I also thank numerous authors for allowing me to reproduce their figures in this review.

## References

- Adler, S. L. 1971, *Annals of Physics*, 67, 599
- Aguilera, D. N., Pons, J. A., & Miralles, J. A. 2008, *A&A*, 486, 255
- Airhart, C., Woods, P. M., Zavlin, V. E., et al. 2008, *40 Years of Pulsars: Millisecond Pulsars, Magnetars and More*, 983, 345
- Akmal, A., Pandharipande, V. R., & Ravenhall, D. G. 1998, *PRC*, 58, 1804
- Alcock, C., Farhi, E., & Olinto, A. 1986, *ApJ*, 310, 261

- Alford, M., Braby, M., Paris, M., & Reddy, S. 2005, *ApJ*, 629, 969
- Alpar, M. A., Cheng, A. F., Ruderman, M. A., & Shaham, J. 1982, *Nature*, 300, 728
- Altamirano, D., Patruno, A., Heinke, C. O., et al. 2010a, *ApJ*, 712, L58
- Altamirano, D., Watts, A., Kalamkar, M., et al. 2010b, *The Astronomer's Telegram*, 2932, 1
- Altamirano, D., Cavecchi, Y., Patruno, A., et al. 2011, *ApJ*, 727, L18
- Anderson, P. W., & Itoh, N. 1975, *Nature*, 256, 25
- Arons, J. 1981, *ApJ*, 248, 1099
- Arras, P., Cumming, A., & Thompson, C. 2004, *ApJ*, 608, L49
- Arzoumanian, Z., Chernoff, D. F., & Cordes, J. M. 2002, *ApJ*, 568, 289
- Bachetti, M., Romanova, M. M., Kulkarni, A., Burderi, L., & di Salvo, T. 2010, *MNRAS*, 403, 1193
- Baldo, M., Bombaci, I., & Burgio, G. F. 1997, *A&A*, 328, 274
- Baldo, M. & Burgio, G. F. 2012, *Rep. Prog. Phys.*, 75, 026301
- Barret, D., Olive, J.-F., & Miller, M. C. 2006, *MNRAS*, 370, 1140
- Bassa, C., Pooley, D., Homer, L., et al. 2004, *ApJ*, 609, 755
- Bauböck, M., Psaltis, D., Özel, F., & Johannsen, T. 2012, *ApJ*, 753, 175
- Becker, W., Swartz, D. A., Pavlov, G. G., et al. 2003, *ApJ*, 594, 798
- Becker, W., & Truemper, J. 1997, *A&A*, 326, 682
- Belian, R. D., Conner, J. P., & Evans, W. D. 1976, *ApJ*, 206, L135
- Bhattacharyya, S., Miller, M. C., & Galloway, D. K. 2010, *MNRAS*, 401, 2
- Bhattacharyya, S., Miller, M. C., & Lamb, F. K. 2006, *ApJ*, 644, 1085
- Bhattacharyya, S., Strohmayer, T. E., Miller, M. C., & Markwardt, C. B. 2005, *ApJ*, 619, 483
- Bildsten, L., Salpeter, E. E., & Wasserman, I. 1992, *ApJ*, 384, 143
- Bogdanov, S., & Grindlay, J. E. 2009, *ApJ*, 703, 1557
- Bogdanov, S., Grindlay, J. E., & Rybicki, G. B. 2006, *ApJ*, 648, L55
- Bogdanov, S., Grindlay, J. E., & Rybicki, G. B. 2008, *ApJ*, 689, 407
- Bogdanov, S., Rybicki, G. B., & Grindlay, J. E. 2007, *ApJ*, 670, 668
- Bogdanov, S., van den Berg, M., Heinke, C. O., et al. 2010, *ApJ*, 709, 241
- Bogdanov, S., van den Berg, M., Servillat, M., et al. 2011, *ApJ*, 730, 81
- Boutelier, M., Barret, D., & Miller, M. C. 2009, *MNRAS*, 399, 1901
- Braje, T. M., & Romani, R. W. 2002, *ApJ*, 580, 1043
- Braje, T. M., Romani, R. W., & Rauch, K. P. 2000, *ApJ*, 531, 447
- Brown, E. F., Bildsten, L., & Chang, P. 2002, *ApJ*, 574, 920
- Brown, E. F., Bildsten, L., & Rutledge, R. E. 1998, *ApJ*, 504, L95
- Brown, E. F., & Cumming, A. 2009, *ApJ*, 698, 1020
- Bulik, T., & Miller, M. C. 1997, *MNRAS*, 288, 596
- Cackett, E. M., Brown, E. F., Cumming, A., Degenaar, N., Miller, J. M., & Wijnands, R. 2010a, *ApJ*, 722, L137
- Cackett, E. M., Brown, E. F., Miller, J. M., & Wijnands, R. 2010b, *ApJ*, 720, 1325
- Cackett, E. M., Fridriksson, J. K., Homan, J., Miller, J. M., & Wijnands, R. 2011, *MNRAS*, 414, 3006
- Cackett, E. M., Miller, J. M., Ballantyne, D. R., et al. 2010c, *ApJ*, 720, 205
- Cackett, E. M., Miller, J. M., Bhattacharyya, S., et al. 2008, *ApJ*, 674, 415
- Cackett et al. 2008, *ApJ*, 687, 87
- Cackett et al. 2006, *MNRAS*, 372, 479
- Cadeau, C., Leahy, D. A., & Morsink, S. M. 2005, *ApJ*, 618, 451
- Cadeau, C., Morsink, S. M., Leahy, D., & Campbell, S. S. 2007, *ApJ*, 654, 458
- Camilo, F., Ransom, S. M., Halpern, J. P., & Reynolds, J. 2007, *ApJ*, 666, L93
- Camilo, F., Ransom, S. M., Halpern, J. P., et al. 2006, *Nature*, 442, 892
- Campana, S., Stella, L., Israel, G., & D'Avanzo, P. 2008, *ApJ*, 689, L129
- Casella, P., Altamirano, D., Patruno, A., Wijnands, R., & van der Klis, M. 2008, *ApJ*, 674, L41
- Chakrabarty, D., Morgan, E. H., Muno, M. P., et al. 2003, *Nature*, 424, 42
- Chang, P., & Bildsten, L. 2003, *ApJ*, 585, 464

- Chang, P., Morsink, S., Bildsten, L., & Wasserman, I. 2006, *ApJ*, 636, L117
- Cook, G. B., Shapiro, S. L., & Teukolsky, S. A. 1994, *ApJ*, 424, 823
- Cooney, A., Dedeo, S., & Psaltis, D. 2010, *PRD*, 82, 064033
- Cottam, J., Paerels, F., & Mendez, M. 2002, *Nature*, 420, 51
- Cumming, A., Arras, P., & Zweibel, E. 2004, *ApJ*, 609, 999
- Damen, E., Magnier, E., Lewin, W. H. G., et al. 1990, *A&A*, 237, 103
- DeDeo, S., & Psaltis, D. 2003, *Physical Review Letters*, 90, 141101
- Degenaar, N., Brown, E. F., & Wijnands, R. 2011a, *MNRAS*, 418, L152
- Degenaar et al. 2011b, *MNRAS*, 412, 1409
- Degenaar, N., & Wijnands, R. 2012, *MNRAS*, 422, 581
- Deliduman, C., Ekşi, K. Y., & Keleş, V. 2012, *JCAP*, 5, 36
- De Luca, A., Caraveo, P. A., Mereghetti, S., Negroni, M., & Bignami, G. F. 2005, *ApJ*, 623, 1051
- Demorest, P. B., Pennucci, T., Ransom, S. M., Roberts, M. S. E., & Hessels, J. W. T. 2010, *Nature*, 467, 1081
- Dib, R., Kaspi, V. M., & Gavriil, F. P. 2007, *ApJ*, 666, 1152
- Dib, R., Kaspi, V. M., & Gavriil, F. P. 2008, *ApJ*, 673, 1044
- Dib, R., Ransom, S. M., Ray, P. S., Kaspi, V. M., & Archibald, A. M. 2005, *ApJ*, 626, 333
- Drake, J. J., Marshall, H. L., Dreizler, S., et al. 2002, *ApJ*, 572, 996
- Elsner, R. F., Heinke, C. O., Cohn, H. N., et al. 2008, *ApJ*, 687, 1019
- Ertan, Ü., Ekşi, K. Y., Erkut, M. H., & Alpar, M. A. 2009, *ApJ*, 702, 1309
- Ertan, Ü., Erkut, M. H., Ekşi, K. Y., & Alpar, M. A. 2007, *ApJ*, 657, 441
- Espinoza, C. M., Lyne, A. G., Stappers, B. W., & Kramer, M. 2011, *MNRAS*, 414, 1679
- Feroci, M., Stella, L., van der Klis, M., et al. 2011, *Experimental Astronomy*, 100
- Fridriksson, J. K., Homan, J., Wijnands, R., et al. 2011, *ApJ*, 736, 162
- Fridriksson et al. 2010, *ApJ*, 714, 270
- Fujimoto, M. Y., Hanawa, T., & Miyaji, S. 1981, *ApJ*, 247, 267
- Fukushima, K., & Hatsuda, T. 2011, *Reports on Progress in Physics*, 74, 014001
- Fushiki, I., & Lamb, D. Q. 1987, *ApJ*, 323, L55
- Gaensler, B. M., & Frail, D. A. 2000, *Nature*, 406, 158
- Galloway, D. K., Chakrabarty, D., Morgan, E. H., & Remillard, R. A. 2002, *ApJL*, 576, L137
- Galloway, D. K., Markwardt, C. B., Morgan, E. H., Chakrabarty, D., & Strohmayer, T. E. 2005, *ApJL*, 622, L45
- Galloway, D. K., Morgan, E. H., Krauss, M. I., Kaaret, P., & Chakrabarty, D. 2007, *ApJL*, 654, L73
- Galloway, D.K., Muno M. P., Hartman J. M., Psaltis D., Chakrabarty D. 2008, *ApJS*, 179, 360
- Galloway, D. K., Psaltis, D., Muno, M. P., & Chakrabarty, D. 2006, *ApJ*, 639, 1033
- Gandolfi, S., Carlson, J., & Reddy, S. 2012, *Phys. Rev. C*, 85, 032801
- Garcia, M. R., McClintock, J. E., Narayan, R., et al. 2001, *ApJL*, 553, L47
- Gavriil, F. P., & Kaspi, V. M. 2002, *ApJ*, 567, 1067
- Gavriil, F. P., Kaspi, V. M., & Woods, P. M. 2002, *Nature*, 419, 142
- Geppert, U., Küker, M., & Page, D. 2004, *A&A*, 426, 267
- Glendenning, N. K. 2000, *Compact stars : nuclear physics, particle physics, and general relativity /*  
Norman K. Glendenning. New York : Springer, 2000
- Glendenning, N. K., & Moszkowski, S. A. 1991, *PRL*, 67, 2414
- Glendenning, N. K., & Schaffner-Bielich, J. 1999, *PRC*, 60, 025803
- Gnedin, I. N., & Pavlov, G. G. 1974, *Zhurnal Eksperimental noi i Teoreticheskoi Fiziki*, 65, 1806
- Göğüş, E., Güver, T., Özel, F., Eichler, D., & Kouveliotou, C. 2011, *ApJ*, 728, 160
- Goldreich, P., & Julian, W. H. 1969, *ApJ*, 157, 869
- Goldreich, P., & Reisenegger, A. 1992, *ApJ*, 395, 250
- Gotthelf, E. V., Perna, R., & Halpern, J. P. 2010, *ApJ*, 724, 1316
- Greenstein, G., & Hartke, G. J. 1983, *ApJ*, 271, 283
- Grindlay, J. E., Camilo, F., Heinke, C. O., et al. 2002, *ApJ*, 581, 470



- Gudmundsson, E. H., Pethick, C. J., & Epstein, R. I. 1983, *ApJ*, 272, 286
- Gudmundsson, E. H., Pethick, C. J., & Epstein, R. I. 1982, *ApJ*, 259, L19
- Guillot, S., Rutledge, R. E., & Brown, E. F. 2011, *ApJ*, 732, 88
- Güver, T., Göğüş, E., Özel, F. 2011, *MNRAS*, 418, 2773
- Güver, T., Özel, F., Göğüş, E. 2008, *ApJ*, 675, 1499
- Güver, T., Özel, F., Göğüş, E., & Kouveliotou, C. 2007, *ApJ*, 667, L73
- Güver, T., Özel, F., Cabrera-Lavers, A., & Wroblewski, P. 2010a, *ApJ*, 712, 964
- Güver, T., Özel, F., & Psaltis, D. 2012a, *ApJ*, 747, 77
- Güver, T., Psaltis, D., Özel, F. 2012b, *ApJ*, 747, 76
- Güver, T., Wroblewski, P., Camarota, L., Özel, F. 2010b, *ApJ*, 719, 1807
- Haberl, F., Motch, C., Zavlin, V. E., et al. 2004, *A&A*, 424, 635
- Haberl, F., Schwobe, A. D., Hambaryan, V., Hasinger, G., & Motch, C. 2003, *A&A*, 403, L19
- Haensel, P., & Zdunik, J. L. 2008, *A&A*, 480, 459
- Haensel, P., & Zdunik, J. L. 1990, *A&A*, 227, 431
- Hailey, C. J., & Mori, K. 2002, *ApJ*, 578, L133
- Halpern, J. P., & Gotthelf, E. V. 2011, *ApJ*, 733, L28
- Hansen, C. J., & van Horn, H. M. 1975, *ApJ*, 195, 735
- Harding, A. K., & Lai, D. 2006, *Reports on Progress in Physics*, 69, 2631
- Harding, A. K., & Muslimov, A. G. 2001, *ApJ*, 556, 987
- Hartman, J. M., Patruno, A., Chakrabarty, D., et al. 2008, *ApJ*, 675, 1468
- Heger, A., Cumming, A., Galloway, D. K., & Woosley, S. E. 2007, *ApJL*, 671, L141
- Heinke, C. O., & Ho, W. C. G. 2010, *ApJL*, 719, L167
- Heinke, C. O., Jonker, P. G., Wijnands, R., & Taam, R. E. 2007, *ApJ*, 660, 1424
- Heinke, C. O., Rybicki, G. B., Narayan, R., & Grindlay, J. E. 2006, *ApJ*, 644, 1090
- Heyl, J. S. 2004, *ApJ*, 600, 939
- Heyl, J. S., & Hernquist, L. 1998, *MNRAS*, 300, 599
- Ho, W. C. G. 2007, *MNRAS* 380, 71
- Ho, W. C. G., & Heinke, C. O. 2009, *Nature*, 462, 71
- Ho, W. C. G., & Lai, D. 2001, *MNRAS*, 327, 1081
- Ho, W. C. G., Lai, D., Potekhin, A. Y., & Chabrier, G. 2003, *ApJ*, 599, 1293
- Hulleman, F., van Kerkwijk, M. H., & Kulkarni, S. R. 2000, *Nature*, 408, 689
- Hulleman, F., Tennant, A. F., van Kerkwijk, M. H., et al. 2001, *ApJ*, 563, L49
- Ibrahim, A. I., Markwardt, C. B., Swank, J. H., et al. 2004, *ApJ*, 609, L21
- Illarionov, A. F., & Sunyaev, R. A. 1975, *A&A*, 39, 185
- Jonker, P. G., Campana, S., Steeghs, D., et al. 2005, *MNRAS*, 361, 511
- Jonker, P. G., Méndez, M., Nelemans, G., Wijnands, R., & van der Klis, M. 2003, *MNRAS*, 341, 823
- Joss, P. C. 1977, *Nature*, 270, 310
- Kaminker, A. D., Pavlov, G. G., & Shibanov, I. A. 1982, *ApSS*, 86, 249
- Kaplan, D. L., Kamble, A., van Kerkwijk, M. H., & Ho, W. C. G. 2011, *ApJ*, 736, 117
- Kaplan, D. L., Kulkarni, S. R., van Kerkwijk, M. H., & Marshall, H. L. 2002, *ApJ*, 570, L79
- Kaplan, D. L., & van Kerkwijk, M. H. 2011, *ApJ*, 740, L30
- Kaplan, D. L., & van Kerkwijk, M. H. 2009, *ApJ*, 692, L62
- Kaplan, D. L., van Kerkwijk, M. H., & Anderson, J. 2007, *ApJ*, 660, 1428
- Kaplan, D. L., van Kerkwijk, M. H., Marshall, H. L., et al. 2003, *ApJ*, 590, 1008
- Kato, M. 1983, *PASJ*, 35, 33
- Kirsch, M. G. F., Mukerjee, K., Breitfellner, M. G., Djavidnia, S., Freyberg, M. J., Kendziorra, E., & Smith, M. J. S. 2004, *A&A*, 423, L9
- Kiziltan, B., Kottas, A., & Thorsett, S. E. 2010, *ApJ*, submitted, arXiv:1011.4291
- Kluzniak, W., Michelson, P., & Wagoner, R. V. 1990, *ApJ*, 358, 538
- Kotake, K., Sato, K., & Takahashi, K. 2006, *Rep. on Prog. in Phys.*, 69, 971
- Kouveliotou, C., Dieters, S., Strohmayer, T., et al. 1998, *Nature*, 393, 235

- Kouveliotou, C., Eichler, D., Woods, P. M., et al. 2003, *ApJ*, 596, L79
- Kramer, M. 2008, *Rev. in Mod. Astr.*, 20, 255
- Kramer, M., & Wex, N 2009, *Classical and Quantum Gravity*, 26, 073001
- Krimm, H. A., et al. 2007, *ApJ*, 668, L147
- Kuiper, L., Hermsen, W., & Mendez, M. 2004, *ApJ*, 613, 1173
- Kuulkers, E., den Hartog, P. R., in't Zand, J. J. M., et al. 2003, *A&A*, 399, 663
- Lamb, D. Q., & Lamb, F. K. 1978, *ApJ*, 220, 291
- Lattimer, J. M., & Prakash, M. 2001, *ApJ*, 550, 426
- Leahy, D. A., Morsink, S. M., & Chou, Y. 2011, *ApJ*, 742, 17
- Leahy, D. A., Morsink, S. M., Chung, Y.-Y., & Chou, Y. 2009, *ApJ*, 691, 1235
- Lin, J., Özel, F., Chakrabarty, D., & Psaltis, D. 2010, *ApJ*, 723, 1053
- Lindblom, L. 1992, *ApJ*, 398, 569
- Link, B., Epstein, R. I., & Lattimer, J. M. 1999, *PRL*, 83, 3362
- Lewin, W. H. G., van Paradijs, J., & Taam, R. E. 1993, *Space Science Reviews*, 62, 223
- Lyutikov, M., & Gavriil, F. P. 2006, *MNRAS*, 368, 690
- Madej, J., Joss, P. C., & Różańska, A. 2004, *ApJ*, 602, 904
- Majczyna, A., Madej, J., Joss, P. C., & Różańska, A. 2005, *A&A*, 430, 643
- Markwardt, C. B., Swank, J. H., Strohmayer, T. E., Zand, J. J. M. i., & Marshall, F. E. 2002, *ApJL*, 575, L21
- Mazets, E. P., & Golenetskii, S. V. 1981, *ApSS*, 75, 47
- Mereghetti, S. 2011a, in *High-Energy Emission from Pulsars and their Systems*, 345, arXiv:1008.2891
- Mereghetti, S. 2011b, *Advances in Space Research*, 47, 1317
- Mészáros, P. 1992, *High-energy radiation from magnetized neutron stars*, University of Chicago Press
- Meszaros, P., & Ventura, J. 1979, *PRD*, 19, 3565
- Miller, M. C. 1995, *ApJ*, 448, L29
- Miller, M. C., & Lamb, F. K. 1998, *ApJ*, 499, L37
- Miller, M. C., Lamb, F. K., & Psaltis, D. 1998, *ApJ*, 508, 791
- Morales, J., Pandharipande, V. R., & Ravenhall, D. G. 2002, *PRC*, 66, 054308
- Mori, K., & Hailey, C. J. 2006, *ApJ*, 648, 1139
- Morsink, S. M., & Leahy, D. A. 2011, *ApJ*, 726, 56
- Morsink, S. M., Leahy, D. A., Cadeau, C., & Braga, J. 2007, *ApJ*, 663, 1244
- Motch, C., Pires, A. M., Haberl, F., Schwobe, A., & Zavlin, V. E. 2009, *A&A*, 497, 423
- Müller, H., & Serot, B. D. 1996, *Nucl. Phys. A*, 606, 508
- Muno, M. P., Özel, F., & Chakrabarty, D. 2002, *ApJ*, 581, 550
- Muno, M. P., Özel, F., & Chakrabarty, D. 2003, *ApJ*, 595, 1066
- Müther, H., Prakash, M., & Ainsworth, T. L. 1987, *Phys. Lett. B*, 199, 469
- Narayan, R., & Cooper, R. L. 2007, *ApJ*, 665, 628
- Narayan, R., & Heyl, J. S. 2003, *ApJ*, 599, 419
- Nath, N. R., Strohmayer, T. E., & Swank, J. H. 2002, *ApJ*, 564, 353
- Ng, C.-Y., Kaspi, V. M., Dib, R., et al. 2011, *ApJ*, 729, 131
- Ögelman, H. 1995 in *Lives of Neutron Stars*, ed. M.A. Alpar, . Kiziloglu and J. van Paradijs, (Kluwer, Dordrecht)
- Özel, F. 2001, *ApJ*, 563, 276
- Özel, F. 2002, *ApJ* 575, 397
- Özel, F. 2003, *ApJ*, 583, 402
- Özel, F. 2004, arXiv:astro-ph/0404144
- Özel, F. 2006, *Nature*, 441, 1115
- Özel, F. 2009, *ApJ*, 691, 1678
- Özel, F., Baym, G., & Güver, T. 2010, *PRD*, 82, 101301
- Özel, F., Gould, A., & Guver, T. 2012, *ApJ*, 748, 5
- Özel, F., Güver, T., Göğüş, E. 2008, *40 Years of Pulsars: Millisecond Pulsars, Magnetars and More*,

- 983, 254
- Özel F., Güver T., & Psaltis D., 2009, *ApJ*, 693, 1775
- Özel, F., & Psaltis, D. 2003, *ApJL*, 582, L31
- Özel, F., & Psaltis, D. 2009, *PRD*, 80, 103003
- Özel, F., Psaltis, D., & Kaspi, V. M. 2001, *ApJ*, 563, 255
- Özel, F., Psaltis, D., Narayan, R., & Santos Villarreal, A. 2012, *ApJ*, in press, arXiv:1201.1006
- Özel, F., Psaltis, D., Ransom, S., Demorest, P., & Alford, M. 2010, *ApJ*, 724, L199
- Paczynski, B. 1983, *ApJ*, 267, 315
- Paczynski, B. 1992, *AcA*, 42, 145
- Page, D. 1995, *ApJ*, 442, 273
- Page, D., Lattimer, J. M., Prakash, M., & Steiner, A. W. 2004, *ApJ Suppl.*, 155, 623
- Page, D., Lattimer, J. M., Prakash, M., & Steiner, A. W. 2009, *ApJ*, 707, 1131
- Page, D., Prakash, M., Lattimer, J. M., & Steiner, A. W. 2011, *PRL*, 106, 081101
- Page, D., & Reddy, S. 2006, *Annual Review of Nuclear and Particle Science*, 56, 327
- Page, D., & Reddy, S. 2012, in *Neutron Star Crust*, ed. C. A. Bertulani and J. Piekarewicz, arXiv:1201.5602
- Page, D., Shibano, Y. A., & Zavlin, V. E. 1995, *ApJ*, 451, L21
- Pannarale, F., Rezzolla, L., Ohme, F., & Read, J. S. 2011, *PRD*, 84, 104017
- Papitto, A., di Salvo, T., Burderi, L., et al. 2007, *MNRAS*, 375, 971
- Papitto, A., Riggio, A., di Salvo, T., et al. 2010, *MNRAS*, 407, 2575
- Patruno, A., Altamirano, D., Hessels, J. W. T., et al. 2009, *ApJ*, 690, 1856
- Pechenick, K. R., Ftaclas, C., & Cohen, J. M. 1983, *ApJ*, 274, 846
- Pérez-Azorín, J. F., Pons, J. A., Miralles, J. A., & Miniutti, G. 2006, *A&A*, 459, 175
- Perna, R., & Gotthelf, E. V. 2008, *ApJ*, 681, 522
- Perna, R., Narayan, R., Rybicki, G., Stella, L., & Treves, A. 2003, *ApJ*, 594, 936
- Pethick, C. J. 1992, *Reviews of Modern Physics*, 64, 1133
- Piro, A. L., & Bildsten, L. 2005, *ApJ*, 629, 438
- Pons, J. A., Walter, F. M., Lattimer, J. M., et al. 2002, *ApJ*, 564, 98
- Potekhin, A. Y., Chabrier, G., & Yakovlev, D. G. 1997, *A&A*, 323, 415
- Poutanen, J., & Gierliński, M. 2003, *MNRAS*, 343, 1301
- Prakash, M., Cooke, J. R., & Lattimer, J. M. 1995, *PRD*, 52, 661
- Psaltis, D. 2008, *Liv. Rev. in Rel.*, 11, 9
- Psaltis, D. 2008, *PRD*, 77, 064006
- Psaltis, D., Belloni, T., & van der Klis, M. 1999, *ApJ*, 520, 262
- Psaltis, D., Özel, F., & DeDeo, S. 2000, *ApJ*, 544, 390
- Radhakrishnan, V., & Srinivasan, G. 1982, *Current Science*, 51, 1096
- Rea, N., Esposito, P., Turolla, R., et al. 2010, *Science*, 330, 944
- Rea, N., Israel, G. L., Turolla, R., et al. 2009, *MNRAS*, 396, 2419
- Rea, N., Zane, S., Turolla, R., Lyutikov, M., Gütz, D. 2008, *ApJ*, 686, 1245
- Read, J. S., Lackey, B. D., Owen, B. J., & Friedman, J. L. 2009, *PRD*, 79, 124032
- Read, J. S., Markakis, C., Shibata, M., et al. 2009, *PRD*, 79, 124033
- Romanova, M. M., Ustyugova, G. V., Koldoba, A. V., & Lovelace, R. V. E. 2004, *ApJ*, 616, L151
- Ruderman, M. A., & Sutherland, P. G. 1975, *ApJ*, 196, 51
- Ruffert, M. 1996, *A&A*, 311, 817
- Rutledge, R. E., Bildsten, L., Brown, E. F., Pavlov, G. G., & Zavlin, V. E. 1999, *ApJ*, 514, 945
- Rutledge, R. E., Bildsten, L., Brown, E. F., Pavlov, G. G., Zavlin, V. E., & Ushomirsky, G. 2002, *ApJ*, 580, 413
- Sanwal, D., Pavlov, G. G., Zavlin, V. E., & Teter, M. A. 2003, *ApJ*, 574, L61
- Schatz, H., et al. 2001, *Physical Review Letters*, 86, 3471
- Shapiro, S. L., & Teukolsky, S. A. 1986, *Black Holes, White Dwarfs and Neutron Stars: The Physics of Compact Objects*, Wiley

- Shternin, P. S., Yakovlev, D. G., Haensel, P., & Potekhin, A. Y. 2007, *MNRAS*, 382, L43
- Shternin, P. S., Yakovlev, D. G., Heinke, C. O., Ho, W. C. G., & Patnaude, D. J. 2011, *MNRAS*, 412, L108
- Slane, P. O., Helfand, D. J., & Murray, S. S. 2002, *ApJL*, 571, L45
- Steiner, A. W., Lattimer, J. M., & Brown, E. F. 2010, *ApJ*, 722, 33
- Stella, L., Vietri, M., & Morsink, S. M. 1999, *ApJ*, 524, L63
- Strohmayer, T., & Bildsten, L. 2006, *Compact stellar X-ray sources*, 113
- Strohmayer, T. E., Zhang, W., & Swank, J. H. 1997, *ApJ*, 487, L77
- Strohmayer, T. E., Zhang, W., Swank, J. H., et al. 1996, *ApJ*, 469, L9
- Suleimanov, V., Poutanen, J., & Werner, K. 2011, *A&A*, 527, A139
- Swank, J. H., Becker, R. H., Boldt, E. A., et al. 1977, *ApJL*, 212, L73
- Takahashi, T., Mitsuda, K., Kelley, R., et al. 2010, *Proc. SPIE*, 7732, 27
- Tetzlaff, N., Schmidt, J. G., Hohle, M. M., & Neuhäuser, R. 2012, *Pubs. Astr. Soc. Austr.*, 29, 98
- Thorne, K. S. 1977, *ApJ*, 212, 825
- Thorsett, S. E., & Chakrabarty, D. 1999, *ApJ*, 512, 288
- Tsai, W.-Y., & Erber, T. 1975, *PRD*, 12, 1132
- Turolla, R., Zane, S., & Drake, J. J. 2004, *ApJ*, 603, 265
- Turon, C., O’Flaherty, K.S., & Perryman, M.A.C. 2005, *The Three-Dimensional Universe with Gaia*, ESA SP-576
- Ulmer, A. 1994, *ApJ*, 437, L111
- van Adelsberg, M., & Lai, D. 2006, *MNRAS*, 373, 1495
- van der Klis, M. 2000, *ARA&A*, 38, 717
- van Kerkwijk, M. H., & Kaplan, D. L. 2007, *ApSS*, 308, 191
- van Kerkwijk, M. H., & Kaplan, D. L. 2008, *ApJ*, 673, L163
- van Kerkwijk, M. H., Kaplan, D. L., Durant, M., Kulkarni, S. R., & Paerels, F. 2004, *ApJ*, 608, 432
- van Paradijs, J. 1978, *Nature*, 274, 650
- van Paradijs, J. 1979, *ApJ*, 234, 609
- van Straaten, S., Ford, E. C., van der Klis, M., Méndez, M., & Kaaret, P. 2000, *ApJ*, 540, 1049
- Wachter, S., Hoard, D. W., Bailyn, C. D., Corbel, S., & Kaaret, P. 2002, *ApJ*, 568, 901
- Wachter, S., Patel, S. K., Kouveliotou, C., et al. 2004, *ApJ*, 615, 887
- Walter, F. M., Eisenbeiß, T., Lattimer, J. M., et al. 2010, *ApJ*, 724, 669
- Wang, Z., Chakrabarty, D., & Kaplan, D. L. 2006, *Nature*, 440, 772
- Wang, Z., Kaspi, V. M., & Higdon, S. J. U. 2007, *ApJ*, 665, 1292
- Watts, A. L., & Strohmayer, T. E. 2007, *APSS*, 308, 625
- Watts, A. L., Strohmayer, T. E., & Markwardt, C. B. 2005, *ApJ*, 634, 547
- Webb, N. A. & Barret, D. 2007, *ApJ*, 671, 727
- Webb, N. A., Olive, J.-F., & Barret, D. 2004, *A&A*, 417, 181
- Weinberg, N., Miller, M. C., & Lamb, D. Q. 2001, *ApJ*, 546, 1098
- Wijnands, R., & van der Klis, M. 1998, *Nature*, 394, 344
- Woods, P. M., Kaspi, V. M., Thompson, C., et al. 2004, *ApJ*, 605, 378
- Woods, P. M., Kouveliotou, C., Göğüş, E., et al. 2001, *ApJ*, 552, 748
- Woods, P. M., & Thompson, C. 2006, *Compact stellar X-ray sources*, 547
- Yakovlev, D. G., Kaminker, A. D., Gnedin, O. Y., & Haensel, P. 2001, *Phys. Rep.*, 354, 1
- Yakovlev, D. G., Ho, W. C. G., Shternin, P. S., Heinke, C. O., & Potekhin, A. Y. 2011, *MNRAS*, 411, 1977
- Yakovlev, D. G., & Pethick, C. J. 2004, *ARA&A*, 42, 169
- Yunes, N., Psaltis, D., Özel, F., & Loeb, A. 2010, *PRD*, 81, 064020
- Zamfir, M., Cumming, A., & Galloway, D. K. 2012, *ApJ*, 749, 69
- Zane, S., Cropper, M., Turolla, R., et al. 2005, *ApJ*, 627, 397
- Zane, S., & Turolla, R. 2006, *MNRAS*, 366, 727
- Zavlin, V. E. 2006, *ApJ*, 638, 951

Zavlin, V. E. 2007, ApSS, 308, 297

Zavlin, V. E., & Pavlov, G. G. 1998, A&A, 329, 583

Zavlin, V. E., Pavlov, G. G., & Shibanov, Y. A. 1996, A&A, 315, 141

Zhang, B., & Harding, A. K. 2000, ApJ, 532, 1150

Zhang, C. M., Wang, J., Zhao, Y. H., et al. 2011, A&A, 527, A83